Title: Unraveling the immunological roles of serum amyloid A3 in aortic immune cell subsets during atherosclerosis progression

Authors: Tzu-Yin Chou[1,2], Yu-Zhen Ye[1,2], I-Jung Lin[1], Chia-Jung Lien[1], Chen-Hsuan Yang[1], Yen-Ting Chen[1], Pei-An Chao[1], Jian-Da Lin[1]*

Affiliations:

[1]Department of Biochemical Science and Technology, National Taiwan University, Taipei 10617, Taiwan

[2]These authors contributed equally.

* Correspondence to:

jdlin@ntu.edu.tw

Abstract

Atherosclerosis is a growing concern in developed nations, necessitating the identification of therapeutic targets for advancing personalized medicine. Serum amyloid A3 (*Saa3*) has been linked to accelerated plaque progression by affecting cholesterol metabolism and modulation of inflammation. We hypothesize that knocking out *Saa3* (*Saa3*$^{-/-}$) could mitigate plaque development by regulating aortic immune cell subsets during atherosclerosis progression. Using a murine model, we induced atherosclerosis via a gain-of-function mutant PCSK9-encoding adeno-associated viral vector (AAVmPCSK9) in wild-type (WT) and *Saa3*$^{-/-}$ mice. Single-cell RNA sequencing revealed that *Saa3*$^{-/-}$ mice developed smaller plaques than WT mice, with significant differences in aortic immune cell populations, particularly aortic macrophages. *Saa3*$^{-/-}$ macrophages, characterized by high *Gpnmb*, *Lpl*, and *Spp1* expressions, predominated over the typical resident foamy macrophages in WT mice. *Saa3*$^{-/-}$ mice also showed enhanced intercellular immune communication and increased signaling interactions, suggesting a shift towards an anti-inflammatory and tissue-repairing phenotype. Our study highlights the potential of *Saa3* as a therapeutic target for atherosclerosis.

35 ## Introduction

36 Atherosclerosis, a major cardiovascular concern in developed countries [1], is a chronic
37 arterial disease characterized by plaque formation within arterial walls. This process
38 involves complex interplays among various cellular components and inflammatory
39 mediators that drive inflammation and lipid accumulation. Atherosclerosis initiation
40 involves low-density lipoprotein (LDL) accumulation in the coronary artery intima,
41 which upon oxidation to ox-LDL by risk factors, activates nuclear factor kappa B (NF-
42 κB) [2,3]. This leads to the expression of adhesion molecules like vascular cell adhesion
43 molecule-1 (VCAM-1) and intercellular adhesion molecule-1 (ICAM-1) on the
44 endothelium, aiding monocyte recruitment into the vascular wall [4]. These recruited
45 monocytes then transform into macrophages under the influence of macrophage
46 colony-stimulating factor (M-CSF), and release inflammatory cytokines such as
47 interleukin (IL)-1β, IL-12, and tumor necrosis factor (TNF)-α, escalating the
48 inflammatory response [5]. Additionally, other immune cells like neutrophils, T cells, and
49 mast cells are recruited to the site. As the disease progresses, these macrophages
50 become foam cells by uptaking ox-LDL, which is crucial for plaque formation and
51 intimal thickening.

52 Macrophages are the predominant type of immune cell found in aortic plaques but

53 display a wide range of phenotypes and functions. At the onset of atherosclerosis,
54 macrophages ingest ox-LDL via receptors like CD36 and SR-A, forming cholesterol-
55 rich foam cells. Continued lipid intake without effective cholesterol removal leads to
56 foam cell death, creating a necrotic core in advanced plaques [6,7]. Single-cell RNA
57 sequencing (scRNA-seq) of monocyte-derived macrophages has revealed that
58 macrophage heterogeneity is beyond M1/M2 definitions and associated with different
59 states of atherosclerosis, where progression is linked to more complex states than
60 regression [8]. This technique has revealed various macrophage subsets within
61 atherosclerotic plaques, each characterized by unique markers and roles contributing to
62 aortic plaque progression or regression. Notably, three main groups are identified:
63 tissue-resident-like macrophages, marked by *Folr2* and *Lyve1*, which promote tissue
64 stability; inflammatory macrophages, with markers such as *Tnf* and *Il1b*, which activate
65 immune responses; and anti-inflammatory TREM2^{hi} macrophages, associated with
66 cholesterol metabolism and identified by markers such as *Trem2* [9,10]. This diversity in
67 macrophage functions underscores the complexity of atherosclerosis and offers
68 multiple targets for therapy.

69 The Serum Amyloid A (SAA) protein family, encompassing SAA3 as one of its
70 members, represents a class of acute phase proteins pivotal in immune responses.
71 Previous studies suggest that *Saa3* has a modulatory role in local injury and

72 inflammatory responses, as the expression of *Saa3* at the mRNA or protein level in
73 mouse macrophages increases with the administered dosage of lipopolysaccharide
74 (LPS) [11]. It also indicates that increased SAA expression correlates with the aortic
75 plaque progression in *ApoE*$^{-/-}$ mice, accompanied by elevated levels of IL-6 and TNF-
76 α. This upregulation potentially facilitates the infiltration of M1 macrophages into
77 atherosclerotic regions, thereby promoting atherosclerosis progression [12]. *Saa3* is
78 actively expressed, predominantly in macrophages and adipose tissues [13], and the
79 activation of the *Saa3* promoter is regulated through C/EBPβ signaling, which in turn
80 activates macrophages, underscoring the complex interaction within adipose tissue [14].
81 Notably, SAA3 has been reported to promote atherosclerosis, and overexpressed SAA3
82 increases atherosclerotic plaque size [15]. Overall, these studies support the role of SAA3
83 in regulating macrophage function during atherosclerosis, though the specific type of
84 aortic macrophages that regulate aortic plaque progression and the underlying
85 mechanisms remain elusive.

86 To assess how *Saa3* deficiency impacts aortic immune cell composition and
87 functionalities in contributing to atherosclerosis progression, we applied scRNA-seq
88 using the BD Rhapsody platform on immune cells from aortic arches of *Saa3* knockout
89 (*Saa3*$^{-/-}$) mice and littermate wild-type (WT) control mice during atherosclerosis. Our
90 investigation seeks to delineate the impact of *Saa3* deficiency on the phenotypic and

91 functional landscape of aortic macrophages and other immune cell populations. By
92 comparing the immune cell profiles between *Saa3*$^{-/-}$ and WT mice, we aim to uncover
93 the molecular mechanisms by which SAA3 influences macrophage or other immune
94 cell types-mediated aortic plaque progression.

95

96 ## Results

97 ### *Saa3* deletion reduced aortic plaque progression but increased peripheral
98 cholesterol levels

99 To determine the phenotype of atherogenesis after *Saa3* deficiency, we utilized a
100 C57BL/6 wild-type (WT) mouse-based atherosclerosis model independent of *Ldlr*$^{-/-}$
101 mice breeding [8,16,17]. Plaque progression was initiated by injecting the mice with an
102 adeno-associated viral vector expressing a gain-of-function mutant of protein
103 convertase subtilisin/kexin type 9 (AAVmPCSK9), resulting in LDL receptor
104 deficiency and hypercholesterolemia. Both C57BL/6 WT and C57BL/6 *Saa3*$^{-/-}$ mice
105 were treated with AAVmPCSK9 and fed a Western diet (WD) for 18 weeks to induce
106 hypercholesterolemia and aortic plaque formation. We longitudinally collected plasma
107 from mice at 0, 2, 4, 8, 12, and 16 weeks on WD, and the immune profiling was
108 performed on sorted CD45+ cells from aortic arches by single-cell RNA-seq at 18
109 weeks on WD (Fig. 1a). We first determined total cholesterol levels in the plasma of
110 WT and *Saa3*$^{-/-}$ mice and a baseline comparison at weeks 0 revealed no significant
111 differences, with levels below 100 mg/dL (Fig. 1b). Over time, *Saa3*$^{-/-}$ mice developed

112 higher cholesterol levels than WT, with a slight increase at weeks 2 through 12, and a
113 significant rise by weeks 16 (Fig. 1b).

114 Research demonstrates that serum amyloid A (SAA) attenuates the anti-
115 inflammatory and antioxidative functions of high-density lipoprotein (HDL) by
116 facilitating its binding to adipocyte and macrophage-derived glycoproteins, thereby
117 compromising its efficacy[18]. We conducted high-density lipoprotein (HDL)/ low-
118 density lipoprotein LDL analyses that revealed an increase in peripheral HDL levels
119 during the initial phase of atherosclerosis progression (Fig. 1c). In *Saa3*$^{-/-}$ mice, not only
120 did HDL levels demonstrate a rising trend with statistically significant increases in the
121 *Saa3*$^{-/-}$ group compared to WT at weeks 2 and 4, but the absence of *Saa3* also correlated
122 with a marked increase in LDL levels in the bloodstream (Fig. 1c).

123 Overexpression or suppression of SAA3 can increase or decrease aortic lesion area
124 in *ApoE*$^{-/-}$ mice[15]. We also determined aortic plaque sizes between WT and *Saa3*$^{-/-}$ mice
125 by histologically evaluating aortic root sections stained with Oil Red O (Fig. 1d). It
126 demonstrated a significant decrease in plaque area in *Saa3*$^{-/-}$ compared to WT mice,
127 with mean values of 31.50% and 45.48%, respectively (Fig. 1e). These observations
128 may support *Saa3* deficiency enhances the circulation of SAA3-free HDL (unmodified
129 HDL), which exhibits pronounced anti-inflammatory properties, potentially mitigating
130 plaque development.

131

132 **_Saa3_ deficiency enhances overall intercellular immune communications in aortic**
133 **arches during atherosclerosis progression**

134 All immune cells express CD45, a major transmembrane glycoprotein expressed on
135 all hematopoietic cells[19] and some cardiac fibroblasts[20]. To elucidate the immunological

136 impact of *Saa3* deficiency within the aortic arch and its putative role in the pathogenesis
137 of atherosclerosis, we performed a single-cell RNA sequencing on FACS-purified
138 CD45+ cells (Supplementary Fig. 1). After data processing, anchor-based dataset
139 integration[21], and cell clusters visualized by Uniform Manifold Approximation and
140 Projection (UMAP), it revealed the cell compositional variances in aortic arches
141 between WT and *Saa3*$^{-/-}$mice during atherosclerosis progression (Fig. 2). Utilizing the
142 cell annotation tool by *SingleR*[22], we classified the cell phenotypes, enabling initial
143 taxonomical segregation within the discerned clusters (Fig. 2a). Our analysis identified
144 11 discrete cell subpopulations, encompassing B cells, dendritic cells (DCs), fibroblasts,
145 innate lymphoid cells (ILCs), macrophages, monocytes, neutrophils, natural killer T
146 (NKT) cells, stromal cells, T cells, and γδ T cells (Tgd) (Fig. 2a). Despite similar UMAP
147 topologies between WT and *Saa3*$^{-/-}$ aortic cell populations (Fig. 2a), *Saa3*$^{-/-}$ mice
148 showed increased T cells, B cells, monocytes, and γδ T cell pro-
149 portions but decreased macrophages, stromal cell, and innate lymphoid cells (ILC)
150 compared to WT mice (Fig. 2b). Heatmaps of differential gene expression profiles
151 supported these *SingleR*-annotated cell type differences, highlighting the top 5 marker
152 genes per subset (Fig. 2c).

153 *Cellchat* has been used to infer, analyze, and visualize cell-cell communication
154 networks in scRNA-seq datasets[22]. To dissect the variances in signaling dynamics in
155 aortic cell types between WT and *Saa3*$^{-/-}$ mice, we employed *CellChat* to evaluate the
156 intercellular communication networks and assess the volume and intensity of cellular
157 interactions within the respective cohorts (Figs. 2d-2f). The resultant metrics
158 demonstrated 3343 and 3857 interactions across all cell types in aortic arches between
159 WT and *Saa3*$^{-/-}$ mice, with interaction strength for *Saa3*$^{-/-}$ cell types quantified at
160 133.288 compared to 97.333 for WT (Fig. 2d). The network graphs elucidate these

161 differential interactions, both in terms of quantity (left) and magnitude (right), among
162 the various cellular phenotypes within the murine aortic microenvironment (Fig. 2e).
163 Interactions augmented in *Saa3*$^{-/-}$ cells are represented by red lines, whilst blue lines
164 indicate more pronounced communication in WT cells, with an observed dominance of
165 red lines suggesting an intensified and potentially more reactive immune milieu in
166 *Saa3*$^{-/-}$ aortae (Fig. 2e). To rigorously dissect the discrete intercellular communication
167 patterns responsible for the observed differential signaling, we interrogate the heatmaps
168 that delineate both the frequency and magnitude of interaction strengths across aortic
169 cell types (Fig. 2f). Increased frequency and magnitude of intercellular interaction
170 strengths were observed in the aortic arches of *Saa3*$^{-/-}$ mice compared to their WT mice
171 (Fig. 2f). We identified a pronounced amplification in signaling pathways, particularly
172 those originating from fibroblasts, macrophages, and stromal cells directed toward
173 neutrophils. The neutrophil subset in the context of *Saa3*$^{-/-}$ mice exhibited a significant
174 enhancement in their interactive roles, acting effectively as both originators and targets
175 of signaling—a contrast to the interaction dynamics evident in the context of WT mice
176 (Fig. 2f). Reversely, there was a tangible suppression of signaling within the cells in
177 aortic arches of *Saa3*$^{-/-}$ mice, as evidenced by reduced communication frequencies from
178 fibroblasts to macrophages and in the macrophage-to-monocyte signaling axis,
179 irrespective of their directional roles in signal propagation (Fig. 2f). These patterns
180 suggest that the absence of the *Saa3* gene exerts a profound regulatory influence on the
181 intercellular communication network among macrophages, monocytes, neutrophils,
182 stromal cells, and fibroblasts, potentially revealing critical insights into the regulatory
183 mechanisms of immune function within the aortic niche.
184

185 ***Saa3* depletion increases biological processes in aortic neutrophils and fibroblasts**

186 **that are highly associated with tissue remodeling during atherosclerosis**

187 *CellChat* analysis revealed significant differences in cell-cell interaction signals
188 between neutrophils within the *Saa3*$^{-/-}$ group compared to the WT (Figs. 2e-2f). To
189 delve deeper, we assessed the transcriptomic variances in neutrophils from WT versus
190 *Saa3*$^{-/-}$ mice. Our volcano plot delineated distinct gene expression profiles, with genes
191 such as *Ncf2*, *Sf3b1*, and *Cd24a* notably upregulated in *Saa3*$^{-/-}$ mice, exceeding the
192 established $\log_2$ fold change threshold of >1 and p-values < 0.01 (Fig. 3a). These genes
193 are critically linked to the production of reactive oxygen species, as well as neutrophil
194 activation and bactericidal functions[23,24]. The observed disparities in gene expression
195 suggest modulated immune responses in *Saa3*$^{-/-}$ aortic neutrophils, potentially
196 influencing their roles in inflammatory processes (Fig. 3a). Further dissection of the
197 phenotypic divergence in neutrophils between WT and *Saa3*$^{-/-}$ mice entailed
198 quantitatively assessing differentially expressed genes (DEGs). Subsequent gene set
199 enrichment analysis, executed via the *ClusterProfiler* package[25], elucidated the
200 predominant gene ontology (GO) pathways impacted by the absence of *Saa3* (Fig. 3b).
201 Compared to WT mice, aortic neutrophils in *Saa3*$^{-/-}$ mice exhibit an upregulation in
202 biological processes encompassing positive regulation of the immune effector process
203 and immune response-activating signaling pathway (Fig. 3b, Supplementary Table 1).

204 The differential gene analysis in fibroblasts between WT and *Saa3*$^{-/-}$ mice revealed
205 significant transcriptional downregulation of *Il6* in the *Saa3*$^{-/-}$ group (Fig. 3c).
206 Consistent with previous reports, IL-6 has been characterized as a pro-inflammatory
207 cytokine that facilitates the trans-differentiation of fibroblasts into myofibroblasts,
208 enhancing chemokine release and immune cell recruitment at inflammation sites [26 27].
209 Conversely, the expression of *Spp1* was upregulated in the *Saa3*$^{-/-}$ fibroblasts,
210 correlating with increased TGF-β expression, collagen production, and fibrosis [28,29].

211 Additionally, elevated expressions of *Col12a1* and *Col5a2* were observed in *Saa3*$^{-/-}$
212 fibroblasts (Fig. 3c), suggesting a propensity towards enhanced tissue remodeling. GO
213 analysis of these enriched genes in aortic fibroblasts from *Saa3*$^{-/-}$ mice highlighted
214 advanced mechanisms of extracellular matrix structuring, organization, and lipid export
215 compared to WT fibroblasts (Fig. 3d, Supplementary Table 1). These alterations in gene
216 expression suggest a modified fibroblast phenotype that may reduce the usual
217 inflammatory response while concurrently enhancing fibrotic repair processes.

218 In comparing the total macrophages from WT and *Saa3*$^{-/-}$ mouse aortic arches, we
219 observed that the absence of *Saa3* markedly alters the gene expression profile within
220 macrophages (Fig. 3e). Notably, genes *Fabp5* and *Gpnmb* are upregulated in *Saa3*$^{-/-}$
221 macrophages (Fig. 3e). *Fabp5*, which plays a central role in the intracellular transport
222 of lipids, is integral to the uptake, transport, and metabolism of fatty acids.[30] *Gpnmb*
223 has been shown to protect against obesity-related metabolic disorders by mitigating
224 macrophage inflammatory capacity[31]. Conversely, genes such as *Cxcl13*, *Lyz1*, *Cp*,
225 *Tmem176a*, *Clec4a1*, *C3*, and *Cfp* are downregulated in *Saa3*$^{-/-}$ macrophages (Fig. 3e).
226 Studies have demonstrated that a lack of *Cxcl13* correlates with a diminished presence
227 of atherosclerotic conditions, likely due to lower recruiting inflammatory granulocytes
228 within the lesions [32 33]. *C3* expression in macrophages has been linked to exacerbating
229 atherosclerosis by limiting macrophage efferocytosis, contributing to plaque
230 development and inflammation.[34] *Cfp* has been linked to regulating complement
231 activation and orchestrating iron homeostasis[35]. Dysregulation or loss of *Cp* gene
232 function precipitates iron overload in these cells, a hallmark of atherogenic
233 macrophages, which consequently accelerates the progression of atherosclerotic
234 disease[36]. Subsequent GO analysis of these enriched genes in aortic macrophages
235 highlighted the increased recruitment and cell chemotaxis in WT mice while *Saa3*$^{-/-}$

236 aortic macrophages increase the lipid localization and transport (Fig. 3f,
237 Supplementary Table 1).

238 Overall, these data suggest that *Saa3* deficiency precipitates states of elevated
239 functional activity within neutrophils and enhances the reparative activity of fibroblasts
240 within the organization, potentially influencing tissue architecture remodeling and
241 reparative capacities that impact aortic plaque progression. The phenotypes of aortic
242 macrophages were impacted by reduced recruitment of inflammatory granulocytes,
243 which helped mitigate inflammation potentially influencing lesion formation and
244 stability.

245

246 **Altered macrophage compositions and enhanced Trem2^{hi} macrophage presence**
247 **linked to diminished aortic plaque progression in *Saa3*$^{-/-}$ mice**

248 Macrophage (Mφ) polarization, along with several distinct clusters, has been
249 identified as increasingly prevalent during the atherosclerosis progression and
250 regression[8,37]. To dissect the functional heterogeneity of aortic macrophage populations
251 in WT and *Saa3*$^{-/-}$ mice during atherosclerosis, we classified macrophages into
252 subpopulations and compared the top differentially expressed genes from each cluster
253 against our previously published dataset, where we profiled single-cell sorted *Cx3cr1*-
254 derived aortic macrophages from lineage-tracing mice during atherosclerosis
255 progression and regression (hereinafter referred to as "*Lin regression study*")[8]. There
256 are five distinct macrophage clusters in the aortic arches of WT and *Saa3*$^{-/-}$ mice during
257 atherosclerosis (Fig. 4a). CD74^{hi}MHCII^{hi} Mφ is the most abundant macrophage subset
258 in both genotypes, with CD74^{hi}MHCII^{hi}, Folr2^{hi}, and Retnla^{hi}Ear2^{hi} Mφ being more
259 prevalent in WT mice compared to *Saa3*$^{-/-}$ mice (Fig. 4b). Conversely, Trem2^{hi} and

260 Apbb2^{hi} Mφ are found in higher percentages within the aortic arches of *Saa3*$^{-/-}$ mice
261 than in WT mice (Fig. 4b).
262 The Cd74^{hi}MHCII^{hi} Mφ, a subset identified through the *Lin regression study*[8], is
263 characterized by high expression of genes such as *Tmem176b*, *Lilra5*, *H2-Eb1*, and *H2-*
264 *Aa* (Supplementary Fig. 2a). Folr2^{hi} Mφ exhibit unique transcriptional profiles with
265 *F13a1, Pf4, Folr2*, and *Lyve1* (Supplementary Fig. 2a). These markers are indicative of
266 a tissue-resident-like macrophage phenotype[38-41] and align with the molecular signature
267 of the Folr2^{hi} macrophage cluster previously delineated in the *Lin regression study* [8].
268 Retnla^{hi}Ear2^{hi} Mφ is distinguished by their elevated expression of genes such as *Retnla*
269 and *Ear2*, which suggest an early-stage transition of monocytes to macrophages within
270 tissues[42,43]. Additionally, these macrophages show enrichment in genes like *Gm2a* and
271 *Fn1*, confirming their specialized state as identified in the *Lin regression study*.[8]
272 Trem2^{hi} Mφ is defined by a gene expression signature that mirrors the population
273 described by *Cochain et al.*[44] and *Lin regression*[8] studies and is exemplified by
274 heightened expression of *Ctsd, Lgals3, Spp1*, and *Lpl* (Supplementary Fig. 2a). Apbb2^{hi}
275 Mφ is characterized by the predominant expression of *Cd9, Cd72*, and *Hexb* genes.
276 While sharing traits with the "Trem2^{hi} Mφ," they are uniquely distinguished by their
277 expression of *Apbb2* (Supplementary Fig. 2a).
278 On the other hand, we identified differentially expressed genes (DEGs) across five
279 macrophage populations and conducted gene ontology (GO) enrichment analysis on
280 biological pathways to explore potential functions (Supplementary Fig. 2b and Table
281 3). Compared to other macrophage clusters, Cd74^{hi}MHCII^{hi} Mφ in the aortic arches
282 showed significant enrichment in pathways related to leukocyte-mediated immunity,
283 positive regulation of cell activation, activation of the immune response, and
284 immunoglobulin-mediated immune responses (Supplementary Fig. 2b and Table 3).

285 Folr2^{hi} Mφ is distinguished by activation of immune response, ameboidal-type cell
286 migration, cell chemotaxis, regulation of angiogenesis, and regulation of viral processes
287 (Supplementary Fig. 2b and Table 3). Retnla^{hi}Ear2^{hi} Mφ were noted for their
288 leukocyte proliferation, mononuclear cell proliferation, positive regulation of leukocyte
289 cell-cell adhesion, positive regulation of T cell activation, and response to type II
290 interferon (Supplementary Fig. 2b and Table 3). Trem2^{hi} Mφ is characterized by a
291 purine ribonucleoside triphosphate biosynthetic process, ATP biosynthetic process,
292 oxidative phosphorylation, aerobic respiration, and the overall generation of precursor
293 metabolites and energy (Supplementary Fig. 2b and Table 3). These functions highlight
294 the metabolic specialization of Trem2^{hi} Mφ in energy production and biosynthesis.
295 Apbb2^{hi} Mφ demonstrated upregulation in myeloid cell differentiation, leukocyte
296 migration, actin filament organization, regulation of protein-containing complex
297 assembly, and mononuclear cell migration (Supplementary Fig. 2b and Table 3).
298 In *Lin regression study*[8], Cd74^{hi}MHCII^{hi} Mφ and Retnla^{hi}Ear2^{hi} Mφ are abundant in
299 aortic arches of progression group and we also observed these two subsets are higher
300 in aortic arches of WT mice compared to *Saa3*$^{-/-}$ mice (Fig. 4b). *Folr2* expression is
301 elevated in human atherosclerotic plaques compared to normal arterial tissue[45] and we
302 also observed aortic Folr2^{hi} Mφ are higher in WT mice than *Saa3*$^{-/-}$ mice (Fig. 4b).
303 Trem2^{hi} Mφ exhibits comparable prevalence between the progression and regression
304 cohorts in the *Lin regression study*[8], whereas both Trem2^{hi} and Apbb2^{hi} Mφ are more
305 abundant in the aortic arches of *Saa3*$^{-/-}$ mice compared to WT mice (Fig. 4b). Trem2^{hi}
306 Mφ is previously identified as lipid-laden foam cells within atherosclerotic lesions,
307 underscoring their capacity for lipid processing and phagocytosis[9,10,37]. They are
308 associated with anti-inflammatory responses, which may help prevent the establishment
309 of a proinflammatory environment within the plaque[9,37,46]. Similar to previous findings,

310 Trem2^{hi} Mφ expresses high *Spp1,* a gene associated with fibrotic responses indicative
311 of tissue repair mechanisms[47,48] (Fig. 4c, Supplementary Fig. 2a). Additionally, this
312 subset expresses *Gpnmb*, a gene implicated in anti-inflammatory processes[31,49], along
313 with *Fabp5*, which is involved in the uptake and transport of fatty acids[30] (Fig. 4c).
314 Notably, enzymes such as *Lpl*, central to lipid metabolism[50] , and *Mmp12*, a contributor
315 to extracellular matrix remodeling[51], further characterize this population. Hence, these
316 data indicate that *Saa3*$^{-/-}$ mice exhibit higher compositions of aortic macrophages with
317 tissue-repairing and anti-inflammatory properties, leading to reduced aortic plaque
318 progression.
319

320 ***Saa3* modulates aortic macrophage functionalities during atherosclerosis**

321 Investigating the transition of macrophage phenotypes from M1-like to M2-like as a
322 therapeutic strategy recognizes the complexity of aortic macrophage phenotypes in
323 atherosclerosis, which extend beyond conventional M1 and M2 polarization states[8,37].
324 We use typical markers for Chemokine, IFN, Inflammatory, and Type II responses to
325 visualize the aortic macrophage subsets from WT and *Saa3*$^{-/-}$ mice (Fig. 4d). Among
326 the comparisons between WT and *Saa3*$^{-/-}$ aortic Mφ, pronounced differences were noted
327 in the increased expression levels of chemokines including *Cxcl1*, *Ccl2*, *Ccl3*, and *Ccl4*
328 in *Saa3*$^{-/-}$ than WT Folr2^{hi} Mφ (Fig. 4d). Chemokines are signaling molecules that
329 attract various types of immune cells to sites of infection or injury. Increased expression
330 of chemokines by tissue-resident macrophages enhances the recruitment of neutrophils
331 and lymphocytes, which is crucial for initiating and sustaining an effective immune
332 response[52]. Additionally, there was a higher expression of type II response markers
333 including *Cd163, Mrc1*, and *Msr1*[53-56] in *Saa3*$^{-/-}$ than WT Folr2^{hi} Mφ (Fig. 4d).

334 Moreover, Il10ra showed higher expression in *Saa3*$^{-/-}$ than WT Cd74^{hi}MHCII^{hi} Mφ, and
335 Il10ra is required for protection against atherosclerosis in low-density lipoprotein
336 receptor knockout mice[57]. Furthermore, we observed higher expression levels of
337 interferon regulatory and downstream markers such as *Irf5*, *Irf7*, *Isg15*, and *Stat1* in
338 WT than *Saa3*$^{-/-}$ Retnla^{hi}Ear2^{hi} Mφ (Figure 4d), which may indicate an enhanced
339 interferon response in these cells [58,59]. These expression patterns indicate a significant
340 alteration in gene expression profiles and macrophage subsets between the two
341 genotypes, suggesting that deletion of the *Saa3* may modulate macrophage recruitment,
342 type 2 immune responses, and inflammatory/anti-inflammatory phenotypes.
343

344 ***Saa3* modulates aortic macrophage communications that impact inflammatory**
345 **processes and aortic plaque compositions**

346 To determine the role of *Saa3* in aortic macrophage communication during
347 atherosclerosis, we also performed a comparative analysis of cell interactions using
348 *CellChat*[22] in both WT and *Saa3*$^{-/-}$ macrophages. Our findings indicate a substantial
349 decline in intercellular communication in *Saa3*$^{-/-}$ macrophages, with interaction events
350 decreasing from 482 in WT to 290 in *Saa3*$^{-/-}$ cells (Fig. 4e). Correspondingly, we
351 observed a significant drop in the strength of these interactions, with the average
352 interaction strength in WT macrophages being 17.997 compared to a lower average of
353 14.348 in *Saa3*$^{-/-}$ macrophages, mirroring the decrease in the number of interaction
354 events (Fig. 4e).

355 The heatmap depicts the overall signaling patterns observed in various macrophage
356 subpopulations from WT and *Saa3*$^{-/-}$ mice (Fig. 4f), and the bar graph shows the relative
357 information flow of these signaling pathways between WT and *Saa3*$^{-/-}$ macrophages
358 (Fig. 4g). In the context of inflammatory-mediated atherosclerosis progression, WT

359 macrophages present higher signaling activity in THBS, ANGPTL, LAMININ, PVR,
360 CD226, OSM, NOTCH, CADAM, and JAM pathways compared to *Saa3*$^{-/-}$
361 macrophages (Figs. 4f-g). In THBS signaling, *Thbs1* is a critical regulator of
362 macrophage interleukin-1β (IL-1β) production and activation via CD47, highlighting
363 the complex interplay between thrombospondins and immune modulation[60]. In
364 ANGPTL signaling, *Angptl2* promotes vascular inflammation and accelerates
365 atherosclerosis progression, with increased cardiac *Angptl2* production linked to heart
366 failure and pathological cardiac remodeling by influencing inflammatory responses and
367 affecting cardiomyocytes and macrophages[61,62]. In LAMININ and JAM signaling,
368 LAMININ and junctional adhesion molecules (JAM) are involved in monocyte-to-
369 macrophage differentiation and macrophage migration, playing roles in immune cell
370 dynamics and atherosclerotic disease modulation[63,64]. PVR significantly contributes to
371 atherosclerosis by facilitating leukocyte migration across the endothelium, thereby
372 promoting inflammation [65]. CD226, a costimulatory molecule, when absent, has been
373 observed to protect against atherosclerosis by preventing foam cell formation and
374 reducing plaque buildup [66]. Oncostatin M (OSM) signaling promotes atherogenesis and
375 plaque vulnerability by promoting the differentiation of vascular smooth muscle cells
376 into osteoblastic phenotypes via M1 macrophages, potentially leading to plaque
377 instability [37]. NOTCH signaling plays a significant role in atherosclerosis development,
378 with *Notch-1* deletion inducing anti-inflammatory M2 effects through the PI3K-Akt
379 pathway, contrasting with its increased presence in vulnerable human plaques [67].
380 In contrast to their WT counterparts, *Saa3*$^{-/-}$ macrophages exhibit elevated expression
381 of signaling molecules such as COLLAGEN, GRN, SN, TGFb, and CLEC. Collagen
382 plays a crucial role in modulating macrophage functions and improving plaque stability,
383 with an increased presence in M2-polarizing macrophages within the plaque [68,69]. GRN

384 exerts anti-atherogenic effects by enhancing nitric oxide production in endothelial cells
385 through the Akt/eNOS signaling pathway, forming a complex with apolipoprotein A-I
386 to stabilize atherosclerotic plaques, and in atherosclerotic mice, its deficiency leads to
387 increased expression of adhesion molecules and inflammatory cytokines[70-72]. TGF-β
388 signaling contributes to the reduction and stabilization of atherosclerotic plaques by
389 altering macrophage behavior, and its overexpression is linked to smaller lesions,
390 increased collagen deposition, smooth muscle cell infiltration, and reduced macrophage
391 presence, ultimately fostering a more stable lesion phenotype[73]. CLEC signaling,
392 specifically through Clec4a2, a C-type lectin receptor, protects against atherosclerosis
393 by promoting homeostatic functions within the vessel wall, enhancing cholesterol
394 metabolism, and limiting immune responses to toll-like receptors [74]. In summary, this
395 analysis confirms that aortic macrophages in WT mice are more associated with
396 inflammatory and migration processes, whereas aortic macrophages in *Saa3*$^{-/-}$ mice are
397 more related to vascular protection and aortic plaque stabilization.
398
399 **Differential effects of *Saa3* deficiency on macrophage subpopulations and ligand-**
400 **receptor interactions**
401 We further investigated the differential effects of *Saa3* deficiency on five
402 macrophage subpopulations. Our observations revealed that, aside from Trem2^{hi} Mφ,
403 the gene expression profiles of CD74^{hi}MHCII^{hi} Mφ, Folr2^{hi} Mφ, Retnla^{hi}Ear2^{hi} Mφ, and
404 Apbb2^{hi} Mφ in *Saa3*$^{-/-}$ mice exhibited substantial downregulation of numerous genes
405 when compared to their WT counterparts (Figs. 5a-d). We also performed GO term
406 enrichment pathway analysis on the downregulated DEGs in these four *Saa3*$^{-/-}$
407 macrophage subpopulations compared to WT (Figs. 5e-h). The analysis revealed
408 common downregulated genes in *Saa3*$^{-/-}$ mice, including *Lyz1*, *Lyz2*, other lysozyme-

409 related genes, *Cxcl13*, and *Ccl8*, which are associated with pathways involved in cell
410 killing and the destruction of other organisms, suggesting that the absence of *Saa3*
411 impairs macrophage functions in combating pathogens as previous studies[75,76] (Figs.
412 5e-h). Specifically, Folr2^{hi} Mφ in *Saa3*$^{-/-}$ mice showed significant downregulation of
413 *Cxcl13* (Fig. 5b). Previous study indicates patients with carotid atherosclerosis exhibit
414 elevated plasma levels of CXCL13, especially in symptomatic cases, and higher
415 CXCL13 expression within atherosclerotic carotid plaques compared to non-
416 atherosclerotic vessels[77]. CCL8 is a potent chemoattractant for monocytes and
417 macrophages, directing them to areas of inflammation and infection[78,79]. Retnla^{hi}Ear2^{hi}
418 Mφ in WT mice show higher enrichment in ERK1 and ERK2 cascade, positive
419 regulation of angiogenesis, and lipid storage (Figs. 5c, 5g). ERK1 and ERK2 signaling
420 pathways regulate macrophage function in atherosclerosis. Deletion of *Erk1* reduces
421 macrophage migration and plaque lipid content in LDL receptor-deficient mice on a
422 high-fat diet[80,81]. Macrophages regulate angiogenesis in atherosclerotic plaques, leading
423 to new blood vessel formation. This enhances lipid and immune cell accumulation,
424 contributing to plaque growth and instability[82]. Apbb2^{hi} Mφ in WT mice enrich in
425 defense response to virus and interferon (Figs. 5d, 5h). This may indicate that WT
426 Apbb2^{hi} Mφ have more inflammatory response features than Saa3$^{-/-}$, contributing to
427 chronic inflammation, plaque instability, and progression [83]. To elucidate the specific
428 ligand-receptor interactions contributing to the observed differences in pathway
429 patterns between *Saa3*$^{-/-}$ and WT groups, we conducted a comparative analysis of
430 ligand-receptor signaling within five subpopulations of macrophages (Supplementary
431 Figs 3a-e). The analysis encompassed an assessment of the differential expression of
432 ligands and receptors and the computation of interaction probabilities, thereby enabling
433 the dissection of signaling discrepancies between the two genotypic conditions. Since

434 aortic Trem2^{hi} Mφs are more abundant in *Saa3*$^{-/-}$ mice, we focus on ligand-receptor
435 interactions within Trem2^{hi} Mφ under both WT and *Saa3*$^{-/-}$ conditions (Supplementary
436 Fig. 3d). Prominently, pairs such as Spp1-Cd44 and Spp1-integrins (Itgav+Itgb1,
437 Itga5+Itgb1, Itga4+Itgb1), exhibit a heightened probability of interaction in the signal
438 transduction pathways of Trem2^{hi} Mφ within the *Saa3*$^{-/-}$ mice (Supplementary Fig. 3d).
439 Spp1 is established to bind integrins Itgav, Itgb1, Itgb5, and Itga4 (Col4a2-Sdc44,
440 Col4a2-Cd44, Col4a2-(Itga9+Itgb1), Col4a1-Sdc44, Col4a1-Cd44, Col4a1-
441 (Itga9+Itgb1)), influencing cellular adhesion and migration crucially[84,85]
442 (Supplementary Fig. 3d). Furthermore, interactions involving Col4a2 and Col4a1 with
443 their partners are exclusively observed in the *Saa3*$^{-/-}$ condition (Supplementary Fig. 3d).
444 As major constituents of the basement membrane, type IV collagen may have
445 implications for the stability of atherosclerotic plaques.[86] In contrast, the CCL-CCR
446 signaling axis, encompassing Ccl9-Ccr1, Ccl8-Ccr1, Ccl7-Ccr1, Ccl6-Ccr2, Ccl6-Ccr1,
447 Ccl3-Ccr5, and Ccl3-Ccr1, is exclusively active in the WT condition within Trem2^{hi}
448 Mφ transitioning to Retnla^{hi}Ear2^{hi} Mφ (Supplementary Fig. 3d). These chemokine-
449 mediated communications facilitate the recruitment of macrophages or monocytes to
450 sites of inflammation, contributing to the formation and progression of atherosclerotic
451 lesions and plaque vulnerability[87,88]. Parallel observations were noted for the ligand-
452 receptor pairs Cd74^{hi}MHCII^{hi} Mφ, Folr2^{hi} Mφ, Retnla^{hi}Ear2^{hi} Mφ, and Apbb2^{hi} Mφ to
453 Retnla^{hi}Ear2^{hi} Mφ (Supplementary Figs. 3a-e). It is posited that these altered signaling
454 patterns may underlie the observed reductions in plaque burden and macrophage
455 recruitments in *Saa3*$^{-/-}$ mice.

456

457 **Trem2^{hi} Mφ potentially mitigates aortic plaque development by enhancing lipid**
458 **absorption, promoting an anti-inflammatory environment, and increasing**
459 **extracellular matrix and fibrosis.**

460 In atherosclerosis, *Saa3* deletion precipitates substantial changes in macrophage gene
461 expression profiles, within the Trem2^{hi} Mφ, as evidenced by differential expression
462 between WT and *Saa3*$^{-/-}$ groups (Fig. 6a). The upregulation of genes in *Saa3*$^{-/-}$ than WT
463 Trem2^{hi} Mφ such as *Fabp4, Fabp5,* and *Lpl*, which are central to lipid metabolism[89,90],
464 as well as *Ctsk* and, has been implicated in promoting disturbed flow-induced
465 endothelial inflammation.[91] Other genes including *Gpnmb, Atp6v0d2, Mrc1, Mmp12*,
466 and *Spp1* also exhibit altered expression (Fig. 6a). Studies suggest that *Gpnmb* may be
467 anti-inflammatory by promoting inflammation resolution, as it can attenuate pro-
468 inflammatory responses and promote M2 polarization in macrophages[49,92,93]. The
469 suppression of *Gpnmb* has been associated with enhanced atherosclerotic plaque
470 formation, whereas its overexpression correlates with decreased plaque development[94].
471 Augmented *Atp6v0d2* expression activates autophagy as a compensatory response to
472 hemodynamic pressure, which indicates its role in maintaining plaque stability and
473 potentially curtailing the progression of atherosclerosis[95,96]. *Mrc1* appears to modulate
474 macrophage polarization toward an anti-inflammatory phenotype[97], while *Mmp12*
475 plays a pivotal role in attenuating inflammation and fostering resolution via targeted
476 proteolysis of chemokines[98,99]. Spp1+ foamy macrophages have been linked to
477 signaling pathways that might abate plaque progression and stabilize susceptible
478 lesions[100]. These genes correspond to GO enrichment pathways such as lipid
479 localization, fatty acid transport, and the positive regulation of macrophage-derived
480 foam cell differentiation (Fig. 6b). These results suggest that *Saa3*$^{-/-}$ Trem2^{hi} Mφ may
481 possess enhanced lipid uptake and metabolism capabilities, which could contribute to

482 the significant reduction in plaque size. Additionally, genes like *Ctsk*, *Gpnmb*, *Igf1*, and
483 *Spp1* are associated with tissue remodeling pathways, indicating a potential shift of
484 *Saa3*$^{-/-}$ Trem2^{hi} Mφ towards an anti-inflammatory phenotype (Fig. 6b). Differential
485 gene expression analysis utilizing violin plots demonstrated that genes associated with
486 tissue repair and lipid metabolism—specifically *Gpnmb*, *Fabp5*, *Lpl, Lgals3*, *Cd36*, and
487 *Spp1*—are more prominently expressed in *Saa3*$^{-/-}$ Trem2^{hi} Mφ compared to their WT
488 counterparts (Fig. 6c). CD36 is a scavenger receptor widely expressed on the surface
489 of various cell types, including macrophages. CD36 binds to oxLDL particles,
490 facilitating their uptake into the macrophage, particularly in the context of
491 atherosclerosis and inflammation[101]. Concomitantly, there is a downregulation of genes
492 in *Saa3*$^{-/-}$ than WT Trem2^{hi} Mφ such as *Thbs1, Kdm7a, Vegfa, Slc7a11, Fn1*, and *Chil3*.
493 These genes correspond to GO enrichment pathways such as positive regulation of
494 chemotaxis, positive regulation of vasculature development, and angiogenesis (Fig. 6b).
495 Angiogenesis is associated with inflammatory cells and can contribute to plaque
496 instability[102,103]. This complex gene expression network underscores the multifaceted
497 influence of *Saa3* in atherosclerosis and pinpoints interconnected genes geared toward
498 modulating macrophage function to combat disease progression.

499 Analysis of aortic Trem2^{hi} macrophages from WT and Saa3$^{-/-}$ mice also revealed a
500 consistent expression pattern for a cohort of genes associated with lipid metabolism and
501 cholesterol processing (Figs 6b-c). The violin plots compare the expression levels of
502 genes central to cholesterol efflux pathways, including *Abca1, Abcg1, Cd36, Nr1h2,*
503 *Scarb1, Pparg, Nr1h3*, and *Apoe* (Fig. 6c, Supplementary Fig. 4). There were no
504 statistically significant differences observed between the two genotypes for most genes;
505 however, an exception was noted in the expression of *Cd36* (Fig. 6c).

506 Analysis through *CellChat* has additionally revealed alterations in the growth
507 differentiation factor (GDF) signaling pathway in all subsets of the aortic macrophages
508 (Figs. 6d-e). In the *Saa3*$^{-/-}$ Trem2^{hi} macrophage phenotype, there is a notable shift
509 towards the sender role in the GDF signaling network (Fig. 6d). In contrast, Folr2^{hi}
510 macrophages predominantly assume the signaling initiative in the WT condition (Figs.
511 6d-e). This shift in signaling behavior suggests that the absence of *Saa3* leads to a
512 reprogramming of the Trem2^{hi} macrophage population, endowing them with a more
513 prominent role in initiating signaling within the GDF pathway. GDF-15 has been
514 reported to reduce cardiac damage and rupture after myocardial infarction by mitigating
515 inflammation and apoptosis via the PI3K/Akt pathway. It also protects against
516 atherosclerosis by modulating apoptosis, inhibiting monocyte recruitment and
517 macrophage activation, and enhancing plaque stability[104-106]. Other studies suggest
518 GDF-15 may reduce macrophage accumulation in *Ldlr*$^{-/-}$ or *Apoe*$^{-/-}$ mice[107-109]. This
519 shift in the gene expression landscape highlights the critical role of *Saa3* in regulating
520 macrophage function and may provide insight into the molecular mechanisms
521 underpinning the immune responses in aortic plaque progression.
522

523 **Discussion**

524 Our study demonstrates that *Saa3* deficiency reduces aortic plaque progression while
525 increasing peripheral cholesterol levels (Figs. 1b-e). This finding aligns with previous
526 research indicating that SAA diminishes the anti-inflammatory and antioxidative
527 capabilities of high-density lipoprotein (HDL) by binding to glycoproteins from
528 adipocytes and macrophages, thereby impairing its anti-inflammatory properties[18,110]. It
529 suggests that serum amyloid A (SAA) compromises HDL functionality, which could
530 explain the elevated cholesterol levels observed in *Saa3*$^{-/-}$ mice. Despite this, *Saa3*$^{-/-}$

531 mice decreased aortic plaque size, indicating that *Saa3* deficiency protects against
532 atherosclerosis (Figs 1d-e).

533 The single-cell RNA sequencing (scRNA-seq) analysis of CD45+ cells from aortic
534 arches revealed significant alterations in the aortic immune cell landscape of *Saa3*$^{-/-}$
535 mice. Increased proportions of T cells, B cells, monocytes, and γδ T cells were noted,
536 while macrophages, stromal cells, and innate lymphoid cells (ILCs) were reduced
537 compared to WT mice (Fig. 2b). This shift in immune cell composition suggests that
538 *Saa3* deficiency alters the inflammatory responses within the aortic arches, potentially
539 contributing to the observed reduction in plaque progression.

540 *CellChat* analysis further highlighted the impact of *Saa3* deficiency on intercellular
541 communication within the aortic microenvironment (Figs. 2, 4). *Saa3*$^{-/-}$ mice exhibited
542 enhanced intercellular interactions, particularly among neutrophils, fibroblasts, and
543 stromal cells, suggesting a more reactive immune milieu. Conversely, a reduced
544 macrophage-to-monocyte and fibroblast-to-macrophage signaling was observed,
545 indicating a dampened inflammatory response (Figure 2d-f). Neutrophils and
546 fibroblasts from *Saa3*$^{-/-}$ mice showed the upregulation of genes associated with immune
547 effector processes and tissue remodeling. Neutrophils exhibited increased expression
548 of genes linked to reactive oxygen species production and bactericidal functions (Fig.
549 3b), while fibroblasts showed enhanced expression of collagen and fibrosis-related
550 genes (Fig. 3d). These findings suggest that *Saa3* deficiency promotes a shift towards a
551 reparative and less inflammatory phenotype in these cell types, potentially influencing
552 atherosclerosis progression.

553 Compared to our previously published dataset, where we profiled single-cell sorted
554 *Cx3cr1*-derived aortic macrophages during atherosclerosis progression and regression[8],
555 we identified 11 aortic macrophage clusters, while we only identified five distinct

556 clusters with notable differences in gene expression between WT and *Saa3*$^{-/-}$ mice (Fig.
557 4a). This may be due to the difference in the platform used to capture single cells
558 between 10X Genomics and BD Rhapsody. Nonetheless, we still observed that Trem2^{hi}
559 macrophages were more abundant in *Saa3*$^{-/-}$ mice (Fig. 4b) and exhibited gene
560 expression profiles indicative of enhanced lipid metabolism and tissue repair functions
561 (Fig. 6). These macrophages may be crucial in mitigating plaque progression by
562 promoting an anti-inflammatory environment and enhancing extracellular matrix
563 production.

564 Our findings also highlight the differential ligand-receptor interactions in WT and
565 *Saa3*$^{-/-}$ mice macrophages (Supplementary Fig. 3). *Saa3* deficiency led to altered
566 signaling dynamics, particularly in Trem2^{hi} macrophages, which showed increased
567 interactions involving *Spp1* and integrins, as well as type IV collagen, suggesting
568 enhanced adhesion and migration capabilities. In contrast, chemokine-mediated
569 communications were more prominent in WT macrophages, facilitating the recruitment
570 of inflammatory cells to atherosclerotic lesions (Supplementary Fig. 3d). The observed
571 changes in gene expression and intercellular communication underscore the complex
572 role of *Saa3* in modulating Trem2^{hi} macrophage functions during atherosclerosis. *Saa3*
573 deficiency appears to shift Trem2^{hi} macrophages towards a phenotype that promotes
574 tissue repair and plaque stability (Fig. 6), which may explain the reduced plaque
575 progression despite elevated cholesterol levels.

576 In conclusion, our study reveals that *Saa3* deficiency has a dual impact on
577 atherosclerosis, reducing aortic plaque progression while increasing peripheral
578 cholesterol levels. The enhanced reparative and anti-inflammatory properties of
579 macrophages, neutrophils, and fibroblasts in *Saa3*$^{-/-}$ mice likely contribute to the
580 observed protective effects against atherosclerosis. These findings provide valuable

581 insights into the regulatory mechanisms of immune function within the aortic niche and
582 highlight the potential of targeting *Saa3* for therapeutic strategies in atherosclerosis.
583 Further research is warranted to elucidate the precise molecular pathways involved and
584 to explore the therapeutic potential of modulating *Saa3* expression in cardiovascular
585 diseases.
586

Author Contributions

TYC, YZY, and JDL designed experiments and interpreted the data. TYC and YZY wrote the manuscript draft, followed by JDL editing. TYC, YZY, IJL, CJL, CHY, YTC, and PAC performed experiments. TYC and YZY coordinated and performed the single-cell RNA-seq experiments and then analyzed single-cell RNA-seq data.

Acknowledgments

We thank the Animal Resource Center and the Consortium of Integrative Biomedical Science Key Technology at National Taiwan University for their technical support.

Funding: This work was financially supported by the National Science and Technology Council, Taiwan (110-2636-B-002-021, 111-2636-B-002-024, 112-2636-B-002-015, 113-2636-B-002-009), National Taiwan University (113L894501, 113-UN0066), Ministry of Education (Yushan Young Fellow Program, Featured Areas Research Center Program of "Center for Advanced Computing and Imaging in Biomedicine" (NTU-113L900701))

605 # Method

606

607 **Animals**

608 All animal procedures were approved by the National Taiwan University IACUC
609 Committee. The Saa3-knockout mice (*Saa3*$^{-/-}$) were developed by the Mutant Mouse
610 Resource & Research Centers (MMRRC). The cryopreserved sperm were acquired and
611 recovered by the National Laboratory Animal Center in Taiwan. We generated
612 heterozygous *Saa3*$^{+/-}$ mice and bred them to obtain 12-week-old Wild-type C57BL/6J
613 mice wild-type (WT) and *Saa3*$^{-/-}$ littermates used for the experiments. Murine
614 atherosclerosis was induced by injecting intraperitoneally once with AAVmPCSK9
615 (ssAAV8/hAAT-mPCSK9D377Y, AAV core, Institute of Biomedical Sciences,
616 Academia Sinica, using a plasmid acquired from Addgene (Plasmid #58376) and kindly
617 provided by Dr. Mi-Hua Tao) at 5×10^{11} viral particles/mouse and fed on Western diet
618 (Research Diets, Cat# D12079Bi) for 18 weeks. All mice were housed in a specific
619 pathogen-free (SPF) environment within individually ventilated cages (IVC) at a
620 ventilation rate of 70-100 air changes per hour (ACH) under positive pressure. The
621 facility maintained a constant temperature of 22 ± 2°C and a relative humidity of 55 ±
622 10%. A 12-hour light-dark cycle was regulated by timers (7:00 AM to 7:00 PM light,
623 7:00 PM to 7:00 AM dark).

624

625 **Cholesterol level measurements**

626 Blood samples were collected from mice and total cholesterol levels in plasma were
627 assessed in WT and *Saa3*$^{-/-}$ mice subjected to AAVmPCSK9D377Y and fed on Western

628 Diet for 0, 4, 8, 12, and 16 weeks (n=5 mice per group). Cholesterol levels were
629 measured using a colorimetric assay (FUJIFILM/Wako, Cat# 639-50981), with
630 absorbance read at 600 nm following a 5-minute incubation at 37 °C. HDL and
631 LDL/VLDL cholesterol levels in plasma were quantified using the ab65390 Cholesterol
632 Assay Kit (Abcam, Version 13a, Updated 17 April 2023), following the manufacturer's
633 protocol with adaptations for our setup. Plasma (20-30 µL) was mixed with an equal
634 volume of 2X Precipitation Buffer to separate the HDL and LDL/VLDL cholesterol
635 fractions. After adding reaction mixes, samples were incubated at 37 °C for 60 minutes
636 away from light. Absorbance was measured at 570 nm using a microplate reader, and
637 cholesterol concentrations were determined by correlating absorbance readings with the
638 standard curve. Statistically significant differences between the two groups at
639 respective time points were determined using the unpaired Mann-Whitney U-test (*$p <$
640 0.05).

641

642 **Histology**

643 At harvesting, the aortic arch was meticulously excised from the experimental mice
644 for the subsequent single-cell isolation, and then aortic roots were embedded in OCT
645 (Catalog # NC0696746). Serial sections were performed at 6 µm on embedded aortic

646 roots and stained with Oil Red O solution (Sigma) for 10 minutes at 37°C. Intimal
647 lesions and stained areas were imaged by an inverted fluorescence microscope
648 (OLYMPUS CKX53) and quantified by ImageJ as previously described [17].
649

650 **Flow cytometry sorting and single-cell RNA-seq library preparation**

651 The protocol for isolating aortic cells from mice is as previously described[8]. Briefly, the
652 procedure began with aorta perfusion using phosphate-buffered saline (PBS). After
653 perfusion, the aortas were stored in FACS buffer. The enzymatic digestion processes
654 involved immersing the aorta in a digestion buffer containing 4U/ml liberase (Roche,
655 Cat. 54001127001), 60U/ml hyaluronidase (Sigma, Cat. H3506), and 40U/ml DNase I
656 (Sigma, Cat. DN25) at specified concentrations, followed by fine mincing. The mixture
657 was incubated at 37°C to facilitate effective digestion, with the process repeated
658 multiple times to ensure complete tissue breakdown. After digestion, the mixture was
659 filtered through a 35μm strainer to obtain a single-cell suspension. The collected cells
660 were then stained with CD45 (Alexa Fluor 488 anti-mouse CD45, Clone: 30-F11,
661 Biolegend, Cat. 103122) and Live/Dead (L/D) Blue markers (Thermo Fisher, Cat.
662 L34962), and the CD45-positive, L/D Blue-negative cells were sorted as
663 Supplementary Figure 1 to prepare single-cell libraries.

664 Single-cell samples were labeled using the BD™ Mouse Immune Single-Cell
665 Multiplexing Kit (Cat. 633793) for each cartridge run on the BD Rhapsody Express
666 Single Cell Analysis System for single-cell capture, followed by cDNA synthesis with
667 the BD Rhapsody cDNA Kit (Cat. 633773). The mRNA Whole Transcriptome Analysis
668 (WTA) and Sample Tag libraries were prepared using the BD Rhapsody™ WTA
669 Amplification Kit (Cat. 633801), according to the manufacturer's guidelines. The
670 quality and quantity of the libraries were assessed using the Agilent 4200 TapeStation
671 System with Agilent High Sensitivity D1000 ScreenTape (Agilent Technologies, Santa
672 Clara, CA) and a Qubit Fluorometer with the Qubit dsDNA HS Assay (Invitrogen, MA,
673 USA). Finally, the libraries were sequenced using the NovaSeq PE150 sequencer
674 (Illumina, San Diego, CA).

675

676 **Reads alignment and single-cell data analysis**

677 The fastq files generated from sequencing were processed using Seven Bridges
678 Genomics. The data were aligned to the mouse_GRCm38-PhiX-gencodevM19-
679 20181206 and demultiplexed using hashtags to separate samples. Subsequent steps
680 included filtering low-quality cells and identifying unique molecule identifiers (UMIs)
681 to produce filtered matrices, which were then utilized as inputs for further analysis. The
682 filtered matrices were analyzed using the Seurat package (v.4.3.0)[111] in R (v.4.3.1).
683 Initially, to exclude low-quality cells, we filtered out cells with nFeature_RNA < 200
684 and percent.mt > 15, tailoring filter parameters for each sample based on violin plots of

685 RNA feature numbers and the percentage of mitochondria in each cell. We used the
686 FindVariableFeatures() function in each sample to select the top 2000 genes with the
687 highest variance using the variance variance-stabilizing transformation (VST) method
688 for downstream analysis. Next, we applied a linear transformation to scale the data,
689 ensuring equal weight to each gene expression level in downstream analysis. A linear
690 dimensional reduction (PCA) was performed, and the Elbow plot was used to decide
691 which PCs to include in the following steps. We cluster cells using the Louvain
692 algorithm (resolution = 0.5). The non-linear dimensional reduction method was
693 employed for visualizing cell clustering, such as UMAP.

694 We followed the Seurat integration analysis pipeline to analyze two or more single-
695 cell datasets together. We used the FindIntegrationAnchors() function to identify
696 anchors, followed by the IntegrateData() function to use these anchors to integrate the
697 datasets. To identify differentially expressed features, we employed the
698 FindAllMarkers() or FindMarkers() functions to identify biomarkers for each cell
699 cluster (min.pct = 0.25, logfc.threshold = 0.25). We used visualization tools such as
700 VlnPlot, feature plot, dotplot, and heatmap to display intergroup gene expression
701 differences. Additionally, to comprehend the potential biological pathway connections
702 of gene sets expressed by each cell population and their differences between two
703 genotypes, we conducted a Gene Ontology (GO) analysis using the ClusterProfiler
704 package (v4.8.3)[112]. This was done after identifying differentially expressed genes
705 (DEGs) in each cell population compared to the cell population of another genotype.
706 The results were visualized using a Dotplot. Moreover, intercellular communications
707 was analyzed using the CellChat package (v1.6.1)[113]. This approach allowed us to
708 understand the roles played by each cell group in signal transduction pathways and

709 compare the differences in cellular signaling among cell groups under different
710 genotypes.

711

712 **Data and code availability**

713 Raw sequence data from single-cell RNA sequencing experiments are deposited in the
714 NCBI Sequence Read Archive under BioProject accession number PRJNA1129034 and
715 gene expression omnibus (GEO) accession number GSE270922. All processing was
716 performed in R and analysis scripts can be found on Github at
717 (https://github.com/JDLinLab/Saa3KO-Arch-scRNAseq-pepline-)

718

719

720

721

722

723

724

725

726

727

728

729

730

731 **Figure legend**

732 **Fig. 1 Effects of *Saa3* deletion on peripheral lipid profiles and aortic plaque**

733 **progression during atherosclerosis.**

734 **(a)** Schematic of an experimental model for the time points of plasma collections and

735 single-cell RNA sequencing (scRNA-seq) on aortic immune cells. C57BL/6 wild-type

736 (WT) and *Saa3*$^{-/-}$ mice were injected with AAVmPCSK9 and fed with the Western diet

737 for 18 weeks. Then aortic arches were digested to single-cell suspensions and FACS-

738 sorted aortic CD45+ cells were subjected to scRNA-seq on the BD Rhapsody platform

739 from WT and *Saa3*$^{-/-}$ mice.

740 **(b)** Plasma total cholesterol levels in WT and *Saa3*$^{-/-}$ mice subjected with

741 ssAAV8/hAAT-mPCSK9 and fed with the Western diet for 0, 4, 8, 12, and 16 weeks.

742 **(c)** Measurement of high-density lipoprotein (HDL) cholesterol levels and low-

743 density lipoprotein (LDL) cholesterol levels in plasma from WT and *Saa3*$^{-/-}$ mice over

744 a period of 0, 2, 4, 8, 12, and 16 weeks.

745 **(d)** Representative Oil Red O staining of aortic root sections in WT and *Saa3*$^{-/-}$ mice at

746 18 weeks post Western diet. Scale bar: 100 μm.

747 **(e)** As in (d), quantification of the lesion area of aortic root sections stained with Oil

748 Red O.

749 All data are presented as mean ± SEM; Statistically significant differences between the

750 two groups at respective time points were denoted by asterisks (*$p < 0.05$), determined

751 using an unpaired Mann-Whitney U-test. Each symbol represents an individual mouse;

752 WT mice (n=5), *Saa3*$^{-/-}$ mice (n=5).

753

754 **Fig. 2 *Saa3* deficiency increases immune intercellular communication in aortic**

755 **arches during atherosclerosis progression.**

756 **(a)** UMAP visualization compares the distribution of cell types in aortic arches between

757 WT and *Saa3*$^{-/-}$ mice. Unbiased cell annotations against the IMMGEN database are

758 colored and labeled accordingly on the plot.

759 **(b)** Cell type composition by percentages of WT and *Saa3*$^{-/-}$ mice (blue, WT; red, *Saa3*$^{-}$

760 $^{/-}$) in total sorted CD45+ cells.

761 **(c)** Heatmap of top 5 marker genes of each cell type in aortic arches from WT and *Saa3*$^{-}$

762 $^{/-}$ mice. The selection of these top marker genes was based on the results of a Wilcoxon

763 test for differential expression.

764 **(d)** Bar plots show the number (left) and strength (right) of inferred interactions of

765 intercellular communication networks in aortic arches from WT and *Saa3*$^{-/-}$ mice.

766 **(e)** Circle plots show the numbers (left) and the strengths (right) of inferred interactions.

767 Node and edge sizes indicate the weights of the inferred networks across WT and *Saa3*-
768 -/- mice. Line color indicates variations between WT and *Saa3*-/- groups, with red
769 showing an increase and blue showing a decrease in interaction numbers within the
770 *Saa3*-/- compared to WT group.

771 **(f)** AS in (e), heatmap visualization of intercellular communication networks in aortic
772 arches from WT and *Saa3*-/- mice. The red and blue colors represent increased or
773 decreased signaling in the aortic arches of *Saa3*-/- mice compared to the WT mice. The
774 top-colored bar plot represents the sum of the columns of values (incoming signaling),
775 and the right-colored bar plot represents the sum of a row of values (outgoing signaling).

776

777 **Fig. 3 Increased fatty acid degradation and oxidative phosphorylation in aortic**
778 **immune cells of *Saa3*-/- mice during atherosclerosis progression.**

779 **(a)**, **(c)**, **(e)** Volcano plot illustrating differential gene expression in neutrophils,
780 fibroblasts, and macrophages within aortic arches of WT versus *Saa3*-/- mice. The x-
781 axis displays the $\log_2$ fold change, while the y-axis shows the -Log_{10} *p*-value. Grey dots
782 denote genes without significant differences, green dots indicate genes with significant
783 fold changes, and red dots mark genes significant in both fold change and *p*-value. The
784 dashed vertical lines represent the fold change boundaries, and the dashed horizontal

785 line demonstrates the p-value significance threshold. Analysis was performed on 26,189

786 genes using DESeq2.

787 **(b)**, **(d)**, **(f)** Top 10 biological processes enriched in neutrophils, fibroblasts, and total

788 macrophages within the aortic arches of WT mice compared to *Saa3*$^{-/-}$ mice (upper

789 panel) or *Saa3*$^{-/-}$ mice compared to wild-type mice (lower panel). Enrichment analysis

790 utilized GO pathways to identify significant biological processes. The gene ratio is

791 plotted along the x-axis, and the enriched biological processes are listed on the y-axis.

792 A color gradient has been applied to indicate the -$\log_{10}$ adjusted *p*-value (p.adjust) of

793 each term, with the size of each point reflecting the number of genes associated with

794 the respective pathway.

795

796 **Fig. 4 Delineation of macrophage sub-cluster in aortic arches between WT and**

797 ***Saa3*$^{-/-}$ mice during atherosclerosis progression.**

798 **(a)** UMAP plots show the sub-clusters of macrophages (Mφ) in aortic arches between

799 WT (left) and *Saa3*$^{-/-}$ (right) mice. Macrophages are delineated based on their gene

800 expression profiles: CD74^{hi}MHCII^{hi} Mφ in navy blue, Folr2^{hi} Mφ in red, Retnla^{hi}Ear2^{hi}

801 Mφ in green, Trem2^{hi} Mφ in sky blue, and Apbb2^{hi} Mφ in pink.

802 **(b)** The bar graph displays the percentage composition of various macrophage

803 subpopulations within total macrophages from WT and *Saa3*$^{-/-}$ mice. Different colors

804 represent distinct macrophage subpopulations as indicated in **(a)**.

805 **(c)** Dot plot representing the expression profiles of five sub-macrophage populations.

806 The x-axis lists genes with differential expression, while the y-axis indicates the sub-

807 macrophage clusters.

808 **(d)** Dot plots show the expression profiles of macrophage markers involved in pathways

809 of chemokine, IFN (interferon), inflammatory, and type II responses across sub-

810 macrophage clusters. For **(c)** and **(d)**, the size of each dot corresponds to the percentage

811 of the indicated cell cluster expressing a particular gene marker, and the color intensity

812 signifies the mean expression level within that cell cluster.

813 **(e)** Bar plots show the number (left) and strength (right) of inferred intercellular

814 communication networks in total aortic macrophages from WT and *Saa3*$^{-/-}$ mice.

815 **(f)** Heatmap visualization of overall signaling patterns in aortic macrophages of WT

816 and *Saa3*$^{-/-}$ mice. The top-colored bar plot represents the sum of each column of values

817 (signaling the strength of overall pathways) across sub-clusters. The gradient blue

818 colored bar represents the relative strength of the indicated pathway.

819 **(g)** The bar graph displays the relative information flow of various signaling molecules

820 in aortic macrophages of WT and *Saa3*$^{-/-}$ mice. Blue bars indicate higher relative

821 information flow in WT macrophages, while red bars indicate higher information flow

822 in *Saa3*$^{-/-}$ macrophages.

823

824 **Fig. 5 *Saa3* deficient impacts gene expression profiles of aortic macrophages**

825 **(a)-(d)** Volcano plot illustrating differential gene expression in four sub-macrophage

826 populations (CD74^{hi} MHCII^{hi} , Folr2^{hi}, Retnla^{hi} Ear2^{hi}, and Apbb2^{hi} macrophage(Mφ))

827 within aortic arches of WT versus *Saa3*$^{-/-}$ mice. The x-axis displays the $\log_2$ fold change,

828 while the y-axis shows the -Log_{10} p-value. Grey dots denote genes without significant

829 differences, green dots indicate genes with significant fold changes, and red dots mark

830 genes significant in both fold change and *p*-value. The dashed vertical lines represent

831 the fold change boundaries, and the dashed horizontal line demonstrates the *p*-value

832 significance threshold. Analysis was performed on 26,189 genes using DESeq2.

833 **(e)-(h)** The bubble plot presents the GO enrichment analysis for CD74^{hi} MHCII^{hi} ,

834 Folr2^{hi}, Retnla^{hi} Ear2^{hi}, and Apbb2^{hi} aortic macrophage (Mφ) from WT and *Saa3*$^{-/-}$ mice.

835 The x-axis represents the GeneRatio. The y-axis lists the enriched GO terms. Bubble

836 size corresponds to the count of DEGs associated with each GO term. The color

837 gradient from blue to red represents the -$\log_{10}$ (adjusted *p*-value) of the enrichment.

838

839 **Fig. 6 Aortic Trem2^{hi} macrophages in *Saa3*$^{-/-}$ mice express more lipid metabolism**

840 **and tissue repair-associated genes.**

841 **(a)** Volcano plot illustrating differential gene expression in aortic Trem2^{hi} macrophage

842 (Mφ) population of WT versus *Saa3*$^{-/-}$ mice.

843 **(b)** The bubble plot presents the GO enrichment analysis for Trem2^{hi} Mφ from WT

844 versus *Saa3*$^{-/-}$ (upper panel) or *Saa3*$^{-/-}$ versus WT (lower panel) mice.

845 **(c)** Violin plots depicting the expression levels of tissue repair-associated genes in

846 Trem2^{hi} Mφ from WT and *Saa3*$^{-/-}$ mice aortas. Each plot indicates the gene expression

847 level for *Gpnmb*, *Fabp5*, *Lpl*, *Lgals3*, *Cd36*, and *Spp1*, with blue representing WT and

848 red for *Saa3*$^{-/-}$ group. The central white bar denotes the median expression level, while

849 the thick bar within the violins indicates the interquartile range. The width of the violins

850 reflects the density of data points at different expression levels.

851 **(d)** The circular diagram illustrates the GDF signaling pathway networks in aortic

852 macrophage subpopulations from WT (left) and *Saa3*$^{-/-}$ (right) mice. Each segment of

853 the circle represents a different macrophage subpopulation. The connections between

854 segments indicate interactions and signaling pathways shared among these

855 subpopulations.

856 **(e)** Heatmap representation of the inferred GDF signaling pathway network across five

sub-populations of aortic macrophages. Each column represents a specific macrophage sub-population, while each row corresponds to the role of the population in the signaling pathway as a sender, receiver, mediator, or influencer.

874 ## Supplementary Figure Legends

875 **Supplementary Fig. 1 Sorting strategy of aortic CD45+ cells.**

876 Flow cytometry analysis was performed for cell sorting to isolate CD45+ immune cells
877 from aortic arches stained for CD45 Alexa 488 and Live/Dead Blue. The top left plot
878 shows forward scatter (FSC-A) versus side scatter (SSC-A), differentiating cells based
879 on size and granularity, with a population gated as P1. The top right plot presents FSC-
880 A versus FSC-H, with the discrimination gate P2 to exclude cell aggregates. The bottom
881 left plot displays SSC-A against the Live/Dead Blue, with live cells gated as P7. The
882 bottom right plot demonstrates SSC-A against the fluorescence intensity of CD45
883 Alexa-488, with the CD45+ population gated as P8. The CD45+ cells were sorted from
884 P8 gated population.

885

886 **Supplementary Fig. 2 Heatmap of top 10 gene markers and GO enrichment**
887 **analysis of five aortic macrophage sub-cluster.**

888 **(a)** Heatmap of top 10 marker genes of each sub-macrophage population in aortic arches
889 from WT and *Saa3*$^{-/-}$ mice. The selection of these top marker genes was based on the
890 results of a Wilcoxon test for differential expression.

891 **(b)** Gene Ontology (GO) enrichment analysis of biological pathways in 5 sub-
892 populations of aortic macrophage (Mφ), using differentially expressed genes (DEGs)
893 identified when comparing one of specific Mφ sub-population against the rest of all
894 other Mφ sub-populations. It can represent the functional characteristics of each Mφ
895 sub-population.

896

897 **Supplementary Fig. 3 Comparison of ligand-receptor pair differences across five**

898 **sub-macrophage populations between WT and *Saa3*$^{-/-}$ mice.**

899 The bubble plot illustrating the protein-protein interaction probabilities between
900 various ligand-receptor pairs across **(a)** CD74^{hi} MHCII^{hi} macrophage (Mφ), **(b)** Folr2^{hi}
901 Mφ, **(c)** Retnla^{hi} Ear2^{hi} Mφ, **(d)** Trem2^{hi} Mφ, and **(e)** Apbb2^{hi} Mφ between WT and
902 *Saa3*$^{-/-}$ mice. The x-axis categorizes the conditions under which the interactions were
903 assessed. The y-axis lists the ligand-receptor pairs. Each bubble's color corresponds to
904 the communication probability, with a gradient from minimum (blue) to maximum (red).
905 The communication probability can be seen as a numerical value representing how
906 strong or likely this interaction is between specific cell types. The size of each bubble
907 represents the *p*-value of the interaction.

908

909 **Supplementary Fig. 4 Comparison of differences in the expression level of**
910 **cholesterol efflux and lipid metabolism genes from Trem2^{hi} macrophages between**
911 **WT and *Saa3*$^{-/-}$ mice.**

912 Differential gene expression in aortic Trem2^{hi} macrophages (Mφ) from WT and *Saa3*$^{-/-}$
913 mice. Violin plots illustrate the distribution of expression levels for genes involved in
914 cholesterol efflux and lipid metabolism in Trem2^{hi} macrophages. Blue represents WT
915 macrophages, while red indicates *Saa3*$^{-/-}$ macrophages.

916

917

918

919

920

921 **Reference**

922 1 Benjamin, E. J. *et al.* Heart Disease and Stroke Statistics-2019 Update: A Report
923 From the American Heart Association. *Circulation* **139**, e56-e528,
924 doi:10.1161/CIR.0000000000000659 (2019).

925 2 Malekmohammad, K., Bezsonov, E. E. & Rafieian-Kopaei, M. Role of Lipid
926 Accumulation and Inflammation in Atherosclerosis: Focus on Molecular and
927 Cellular Mechanisms. *Front Cardiovasc Med* **8**, 707529,
928 doi:10.3389/fcvm.2021.707529 (2021).

929 3 Libby, P. *et al.* Atherosclerosis. *Nat Rev Dis Primers* **5**, 56, doi:10.1038/s41572-
930 019-0106-z (2019).

931 4 Steinl, D. C. & Kaufmann, B. A. Ultrasound imaging for risk assessment in
932 atherosclerosis. *Int J Mol Sci* **16**, 9749-9769, doi:10.3390/ijms16059749 (2015).

933 5 Sekalska, B. [Aortic expression of monocyte chemotactic protein-1 (MCP-1)
934 gene in rabbits with experimental atherosclerosis]. *Ann Acad Med Stetin* **49**, 79-
935 90 (2003).

936 6 Zhang, Y. *et al.* Oxidized high-density lipoprotein promotes CD36
937 palmitoylation and increases lipid uptake in macrophages. *J Biol Chem* **298**,
938 102000, doi:10.1016/j.jbc.2022.102000 (2022).

939 7 Javadifar, A. *et al.* Foam Cells as Therapeutic Targets in Atherosclerosis with a
940 Focus on the Regulatory Roles of Non-Coding RNAs. *Int J Mol Sci* **22**,
941 doi:10.3390/ijms22052529 (2021).

942 8 Lin, J. D. *et al.* Single-cell analysis of fate-mapped macrophages reveals
943 heterogeneity, including stem-like properties, during atherosclerosis
944 progression and regression. *JCI Insight* **4**, doi:10.1172/jci.insight.124574
945 (2019).

946 9 Zhang, K. *et al.* TREM2(hi) resident macrophages protect the septic heart by
947 maintaining cardiomyocyte homeostasis. *Nat Metab* **5**, 129-146,
948 doi:10.1038/s42255-022-00715-5 (2023).

949 10 Jung, S. H. *et al.* Spatiotemporal dynamics of macrophage heterogeneity and a
950 potential function of Trem2(hi) macrophages in infarcted hearts. *Nat Commun*
951 **13**, 4580, doi:10.1038/s41467-022-32284-2 (2022).

952 11 Reigstad, C. S., Lunden, G. O., Felin, J. & Backhed, F. Regulation of serum
953 amyloid A3 (SAA3) in mouse colonic epithelium and adipose tissue by the

954 intestinal microbiota. *PLoS One* **4**, e5842, doi:10.1371/journal.pone.0005842
955 (2009).

956 12 Dong, Z. *et al.* Serum amyloid A directly accelerates the progression of
957 atherosclerosis in apolipoprotein E-deficient mice. *Mol Med* **17**, 1357-1364,
958 doi:10.2119/molmed.2011.00186 (2011).

959 13 Meek, R. L., Eriksen, N. & Benditt, E. P. Murine serum amyloid A3 is a high
960 density apolipoprotein and is secreted by macrophages. *Proc Natl Acad Sci U S*
961 *A* **89**, 7949-7952, doi:10.1073/pnas.89.17.7949 (1992).

962 14 Sanada, Y. *et al.* Serum Amyloid A3 Gene Expression in Adipocytes is an
963 Indicator of the Interaction with Macrophages. *Sci Rep* **6**, 38697,
964 doi:10.1038/srep38697 (2016).

965 15 Thompson, J. C. *et al.* Serum amyloid A3 is pro-atherogenic. *Atherosclerosis*
966 **268**, 32-35, doi:10.1016/j.atherosclerosis.2017.11.011 (2018).

967 16 Keeter, W. C., Carter, N. M., Nadler, J. L. & Galkina, E. V. The AAV-PCSK9
968 murine model of atherosclerosis and metabolic dysfunction. *Eur Heart J Open*
969 **2**, oeac028, doi:10.1093/ehjopen/oeac028 (2022).

970 17 Peled, M. *et al.* A wild-type mouse-based model for the regression of
971 inflammation in atherosclerosis. *PLoS One* **12**, e0173975,
972 doi:10.1371/journal.pone.0173975 (2017).

973 18 Han, C. Y. *et al.* Serum amyloid A-containing HDL binds adipocyte-derived
974 versican and macrophage-derived biglycan, reducing its antiinflammatory
975 properties. *JCI Insight* **5**, doi:10.1172/jci.insight.142635 (2020).

976 19 Holmes, N. CD45: all is not yet crystal clear. *Immunology* **117**, 145-155,
977 doi:10.1111/j.1365-2567.2005.02265.x (2006).

978 20 Haudek, S. B. *et al.* Bone marrow-derived fibroblast precursors mediate
979 ischemic cardiomyopathy in mice. *Proc Natl Acad Sci U S A* **103**, 18284-18289,
980 doi:10.1073/pnas.0608799103 (2006).

981 21 Stuart, T. *et al.* Comprehensive Integration of Single-Cell Data. *Cell* **177**, 1888-
982 1902 e1821, doi:10.1016/j.cell.2019.05.031 (2019).

983 22 Aran, D. *et al.* Reference-based analysis of lung single-cell sequencing reveals
984 a transitional profibrotic macrophage. *Nat Immunol* **20**, 163-172,
985 doi:10.1038/s41590-018-0276-y (2019).

986 23 Gowdy, K. M. *et al.* Key role for scavenger receptor B-I in the integrative

987 physiology of host defense during bacterial pneumonia. *Mucosal Immunol* **8**,
988 559-571, doi:10.1038/mi.2014.88 (2015).

989 24 Sawant, K. V. *et al.* Neutrophil recruitment by chemokines Cxcl1/KC and
990 Cxcl2/MIP2: Role of Cxcr2 activation and glycosaminoglycan interactions. *J*
991 *Leukoc Biol* **109**, 777-791, doi:10.1002/JLB.3A0820-207R (2021).

992 25 Wu, T. *et al.* clusterProfiler 4.0: A universal enrichment tool for interpreting
993 omics data. *Innovation (Camb)* **2**, 100141, doi:10.1016/j.xinn.2021.100141
994 (2021).

995 26 Hwang, S. Y. *et al.* IL-17 induces production of IL-6 and IL-8 in rheumatoid
996 arthritis synovial fibroblasts via NF-kappaB- and PI3-kinase/Akt-dependent
997 pathways. *Arthritis Res Ther* **6**, R120-128, doi:10.1186/ar1038 (2004).

998 27 Zongfei, J. *et al.* In vitro IL-6/IL-6R Trans-Signaling in Fibroblasts Releases
999 Cytokines That May Be Linked to the Pathogenesis of IgG4-Related Disease.
1000 *Front Immunol* **11**, 1272, doi:10.3389/fimmu.2020.01272 (2020).

1001 28 Kramerova, I. *et al.* Spp1 (osteopontin) promotes TGFbeta processing in
1002 fibroblasts of dystrophin-deficient muscles through matrix metalloproteinases.
1003 *Hum Mol Genet* **28**, 3431-3442, doi:10.1093/hmg/ddz181 (2019).

1004 29 Dong, J. & Ma, Q. Osteopontin enhances multi-walled carbon nanotube-
1005 triggered lung fibrosis by promoting TGF-beta1 activation and myofibroblast
1006 differentiation. *Part Fibre Toxicol* **14**, 18, doi:10.1186/s12989-017-0198-0
1007 (2017).

1008 30 Xu, B. *et al.* The Biological Functions and Regulatory Mechanisms of Fatty
1009 Acid Binding Protein 5 in Various Diseases. *Front Cell Dev Biol* **10**, 857919,
1010 doi:10.3389/fcell.2022.857919 (2022).

1011 31 Nickl, B., Qadri, F. & Bader, M. Anti-inflammatory role of Gpnmb in adipose
1012 tissue of mice. *Sci Rep* **11**, 19614, doi:10.1038/s41598-021-99090-6 (2021).

1013 32 Ding, C. *et al.* The Teleost CXCL13-CXCR5 Axis Induces Inflammatory
1014 Cytokine Expression through the Akt-NF-kappaB, p38-AP-1, and p38-NF-
1015 kappaB Pathways. *J Immunol* **212**, 317-334, doi:10.4049/jimmunol.2300237
1016 (2024).

1017 33 Han, J. H. *et al.* Association of CXCL10 and CXCL13 levels with disease
1018 activity and cutaneous manifestation in active adult-onset Still's disease.
1019 *Arthritis Res Ther* **17**, 260, doi:10.1186/s13075-015-0773-4 (2015).

1020 34 Kiss, M. G. *et al.* Cell-autonomous regulation of complement C3 by factor H

1021 limits macrophage efferocytosis and exacerbates atherosclerosis. *Immunity* **56**,
1022 1809-1824 e1810, doi:10.1016/j.immuni.2023.06.026 (2023).

1023 35 Suzuki, M. *et al.* Cholesterol accumulation regulates expression of macrophage
1024 proteins implicated in proteolysis and complement activation. *Arterioscler*
1025 *Thromb Vasc Biol* **32**, 2910-2918, doi:10.1161/ATVBAHA.112.300383 (2012).

1026 36 Marques, L., Negre-Salvayre, A., Costa, L. & Canonne-Hergaux, F. Iron gene
1027 expression profile in atherogenic Mox macrophages. *Biochim Biophys Acta*
1028 **1862**, 1137-1146, doi:10.1016/j.bbadis.2016.03.004 (2016).

1029 37 Hou, P. *et al.* Macrophage polarization and metabolism in atherosclerosis. *Cell*
1030 *Death Dis* **14**, 691, doi:10.1038/s41419-023-06206-z (2023).

1031 38 Cochain, C. *et al.* Single-Cell RNA-Seq Reveals the Transcriptional Landscape
1032 and Heterogeneity of Aortic Macrophages in Murine Atherosclerosis. *Circ Res*
1033 **122**, 1661-1674, doi:10.1161/CIRCRESAHA.117.312509 (2018).

1034 39 Nalio Ramos, R. *et al.* Tissue-resident FOLR2(+) macrophages associate with
1035 CD8(+) T cell infiltration in human breast cancer. *Cell* **185**, 1189-1207 e1125,
1036 doi:10.1016/j.cell.2022.02.021 (2022).

1037 40 Ensan, S. *et al.* Self-renewing resident arterial macrophages arise from
1038 embryonic CX3CR1(+) precursors and circulating monocytes immediately after
1039 birth. *Nat Immunol* **17**, 159-168, doi:10.1038/ni.3343 (2016).

1040 41 Beckers, C. M. L. *et al.* Cre/lox Studies Identify Resident Macrophages as the
1041 Major Source of Circulating Coagulation Factor XIII-A. *Arterioscler Thromb*
1042 *Vasc Biol* **37**, 1494-1502, doi:10.1161/ATVBAHA.117.309271 (2017).

1043 42 Sanin, D. E. *et al.* A common framework of monocyte-derived macrophage
1044 activation. *Sci Immunol* **7**, eabl7482, doi:10.1126/sciimmunol.abl7482 (2022).

1045 43 Loke, P. & Lin, J. D. Redefining inflammatory macrophage phenotypes across
1046 stages and tissues by single-cell transcriptomics. *Sci Immunol* **7**, eabo4652,
1047 doi:10.1126/sciimmunol.abo4652 (2022).

1048 44 Cochain, C. *et al.* Single-Cell RNA-Seq Reveals the Transcriptional Landscape
1049 and Heterogeneity of Aortic Macrophages in Murine Atherosclerosis. *Circ Res*
1050 **122**, 1661-1674, doi:CIRCRESAHA.117.312509 [pii]

1051 10.1161/CIRCRESAHA.117.312509 (2018).

1052 45 Muller, A. *et al.* Imaging atherosclerotic plaque inflammation via folate receptor
1053 targeting using a novel 18F-folate radiotracer. *Mol Imaging* **13**, 1-11 (2014).

1054 46 Kim, K. *et al.* Transcriptome Analysis Reveals Nonfoamy Rather Than Foamy
1055 Plaque Macrophages Are Proinflammatory in Atherosclerotic Murine Models.
1056 *Circ Res* **123**, 1127-1142, doi:10.1161/CIRCRESAHA.118.312804 (2018).

1057 47 Qi, J. *et al.* Single-cell and spatial analysis reveal interaction of FAP(+)
1058 fibroblasts and SPP1(+) macrophages in colorectal cancer. *Nat Commun* **13**,
1059 1742, doi:10.1038/s41467-022-29366-6 (2022).

1060 48 Hoeft, K. *et al.* Platelet-instructed SPP1(+) macrophages drive myofibroblast
1061 activation in fibrosis in a CXCL4-dependent manner. *Cell Rep* **42**, 112131,
1062 doi:10.1016/j.celrep.2023.112131 (2023).

1063 49 Saade, M., Araujo de Souza, G., Scavone, C. & Kinoshita, P. F. The Role of
1064 GPNMB in Inflammation. *Front Immunol* **12**, 674739,
1065 doi:10.3389/fimmu.2021.674739 (2021).

1066 50 Kumari, A., Kristensen, K. K., Ploug, M. & Winther, A. L. The Importance of
1067 Lipoprotein Lipase Regulation in Atherosclerosis. *Biomedicines* **9**,
1068 doi:10.3390/biomedicines9070782 (2021).

1069 51 Wang, X. & Khalil, R. A. Matrix Metalloproteinases, Vascular Remodeling, and
1070 Vascular Disease. *Adv Pharmacol* **81**, 241-330,
1071 doi:10.1016/bs.apha.2017.08.002 (2018).

1072 52 Zou, Y. *et al.* Nrf2 is essential for timely M phase entry of replicating
1073 hepatocytes during liver regeneration. *Am J Physiol Gastrointest Liver Physiol*
1074 **308**, G262-268, doi:10.1152/ajpgi.00332.2014 (2015).

1075 53 Buechler, C. *et al.* Regulation of scavenger receptor CD163 expression in
1076 human monocytes and macrophages by pro- and antiinflammatory stimuli. *J*
1077 *Leukoc Biol* **67**, 97-103 (2000).

1078 54 Martinez, F. O. & Gordon, S. The M1 and M2 paradigm of macrophage
1079 activation: time for reassessment. *F1000Prime Rep* **6**, 13, doi:10.12703/P6-13
1080 (2014).

1081 55 Gudgeon, J., Marin-Rubio, J. L. & Trost, M. The role of macrophage scavenger
1082 receptor 1 (MSR1) in inflammatory disorders and cancer. *Front Immunol* **13**,
1083 1012002, doi:10.3389/fimmu.2022.1012002 (2022).

1084 56 Zhao, S. J. *et al.* Macrophage MSR1 promotes BMSC osteogenic differentiation
1085 and M2-like polarization by activating PI3K/AKT/GSK3beta/beta-catenin
1086 pathway. *Theranostics* **10**, 17-35, doi:10.7150/thno.36930 (2020).

1087 57 Kurilenko, N., Fatkhullina, A. R., Mazitova, A. & Koltsova, E. K. Act Locally,

1088 Act Globally-Microbiota, Barriers, and Cytokines in Atherosclerosis. *Cells* **10**,
1089 doi:10.3390/cells10020348 (2021).

1090 58 Chen, H. J., Tas, S. W. & de Winther, M. P. J. Type-I interferons in
1091 atherosclerosis. *J Exp Med* **217**, doi:10.1084/jem.20190459 (2020).

1092 59 Edsfeldt, A. *et al.* Interferon regulatory factor-5-dependent CD11c+
1093 macrophages contribute to the formation of rupture-prone atherosclerotic
1094 plaques. *Eur Heart J* **43**, 1864-1877, doi:10.1093/eurheartj/ehab920 (2022).

1095 60 Stein, E. V., Miller, T. W., Ivins-O'Keefe, K., Kaur, S. & Roberts, D. D. Secreted
1096 Thrombospondin-1 Regulates Macrophage Interleukin-1beta Production and
1097 Activation through CD47. *Sci Rep* **6**, 19684, doi:10.1038/srep19684 (2016).

1098 61 Tian, Z. *et al.* ANGPTL2 activity in cardiac pathologies accelerates heart failure
1099 by perturbing cardiac function and energy metabolism. *Nat Commun* **7**, 13016,
1100 doi:10.1038/ncomms13016 (2016).

1101 62 Horio, E. *et al.* Role of endothelial cell-derived angptl2 in vascular
1102 inflammation leading to endothelial dysfunction and atherosclerosis
1103 progression. *Arterioscler Thromb Vasc Biol* **34**, 790-800,
1104 doi:10.1161/ATVBAHA.113.303116 (2014).

1105 63 Li, L. *et al.* Endothelial Basement Membrane Laminins as an Environmental
1106 Cue in Monocyte Differentiation to Macrophages. *Front Immunol* **11**, 584229,
1107 doi:10.3389/fimmu.2020.584229 (2020).

1108 64 Wang, J. & Liu, H. The Roles of Junctional Adhesion Molecules (JAMs) in Cell
1109 Migration. *Front Cell Dev Biol* **10**, 843671, doi:10.3389/fcell.2022.843671
1110 (2022).

1111 65 Mishra, B. H. *et al.* Modular genome-wide gene expression architecture shared
1112 by early traits of osteoporosis and atherosclerosis in the Young Finns Study. *Sci*
1113 *Rep* **11**, 7111, doi:10.1038/s41598-021-86536-0 (2021).

1114 66 Zhang, Y. *et al.* Loss of CD226 protects apolipoprotein E-deficient mice from
1115 diet-induced atherosclerosis. *Biochim Biophys Acta Mol Basis Dis* **1868**,
1116 166452, doi:10.1016/j.bbadis.2022.166452 (2022).

1117 67 Zhang, M. *et al.* Macrophage-specific deletion of Notch-1 induced M2 anti-
1118 inflammatory effect in atherosclerosis via activation of the PI3K-oxidative
1119 stress axis. *Aging (Albany NY)* **15**, 15196-15212, doi:10.18632/aging.205342
1120 (2023).

1121 68 Barrett, T. J. Macrophages in Atherosclerosis Regression. *Arterioscler Thromb*

1122 *Vasc Biol* **40**, 20-33, doi:10.1161/ATVBAHA.119.312802 (2020).

1123 69 Scott, T. E. *et al.* IL-4 and IL-13 induce equivalent expression of traditional M2
1124 markers and modulation of reactive oxygen species in human macrophages. *Sci*
1125 *Rep* **13**, 19589, doi:10.1038/s41598-023-46237-2 (2023).

1126 70 Huang, G. *et al.* Potential role of full-length and nonfull-length progranulin in
1127 affecting aortic valve calcification. *J Mol Cell Cardiol* **141**, 93-104,
1128 doi:10.1016/j.yjmcc.2020.03.012 (2020).

1129 71 Saeedi-Boroujeni, A. *et al.* Progranulin (PGRN) as a regulator of inflammation
1130 and a critical factor in the immunopathogenesis of cardiovascular diseases. *J*
1131 *Inflamm (Lond)* **20**, 1, doi:10.1186/s12950-023-00327-0 (2023).

1132 72 Nguyen, A. D. *et al.* Progranulin in the hematopoietic compartment protects
1133 mice from atherosclerosis. *Atherosclerosis* **277**, 145-154,
1134 doi:10.1016/j.atherosclerosis.2018.08.042 (2018).

1135 73 Reifenberg, K. *et al.* Overexpression of TGF-ss1 in macrophages reduces and
1136 stabilizes atherosclerotic plaques in ApoE-deficient mice. *PLoS One* **7**, e40990,
1137 doi:10.1371/journal.pone.0040990 (2012).

1138 74 Park, I. *et al.* C-type lectin receptor CLEC4A2 promotes tissue adaptation of
1139 macrophages and protects against atherosclerosis. *Nat Commun* **13**, 215,
1140 doi:10.1038/s41467-021-27862-9 (2022).

1141 75 Chauvin, C. *et al.* Loss of NOD2 in macrophages improves colitis and
1142 tumorigenesis in a lysozyme-dependent manner. *Front Immunol* **14**, 1252979,
1143 doi:10.3389/fimmu.2023.1252979 (2023).

1144 76 Alam, M. S. *et al.* Genomic expression analyses reveal lysosomal, innate
1145 immunity proteins, as disease correlates in murine models of a lysosomal
1146 storage disorder. *PLoS One* **7**, e48273, doi:10.1371/journal.pone.0048273
1147 (2012).

1148 77 Smedbakken, L. M. *et al.* Increased levels of the homeostatic chemokine
1149 CXCL13 in human atherosclerosis - Potential role in plaque stabilization.
1150 *Atherosclerosis* **224**, 266-273, doi:10.1016/j.atherosclerosis.2012.06.071
1151 (2012).

1152 78 Dangi, A. *et al.* Blocking CCL8-CCR8-Mediated Early Allograft Inflammation
1153 Improves Kidney Transplant Function. *J Am Soc Nephrol* **33**, 1876-1890,
1154 doi:10.1681/ASN.2022020139 (2022).

1155 79 Luo, H., Li, L., Han, S. & Liu, T. The role of monocyte/macrophage chemokines

1156 in pathogenesis of osteoarthritis: A review. *Int J Immunogenet* **51**, 130-142,
1157 doi:10.1111/iji.12664 (2024).

1158 80 Ricard, N., Zhang, J., Zhuang, Z. W. & Simons, M. Isoform-Specific Roles of
1159 ERK1 and ERK2 in Arteriogenesis. *Cells* **9**, doi:10.3390/cells9010038 (2019).

1160 81 Al-Ahmadi, W. *et al.* Pro-atherogenic actions of signal transducer and activator
1161 of transcription 1 serine 727 phosphorylation in LDL receptor deficient mice
1162 via modulation of plaque inflammation. *FASEB J* **35**, e21892,
1163 doi:10.1096/fj.202100571RR (2021).

1164 82 Theofilis, P., Oikonomou, E., Tsioufis, K. & Tousoulis, D. The Role of
1165 Macrophages in Atherosclerosis: Pathophysiologic Mechanisms and Treatment
1166 Considerations. *Int J Mol Sci* **24**, doi:10.3390/ijms24119568 (2023).

1167 83 Jin, M. *et al.* Regulation of toll-like receptor (TLR) signaling pathways in
1168 atherosclerosis: from mechanisms to targeted therapeutics. *Acta Pharmacol Sin*
1169 **44**, 2358-2375, doi:10.1038/s41401-023-01123-5 (2023).

1170 84 Frank, J. W., Seo, H., Burghardt, R. C., Bayless, K. J. & Johnson, G. A. ITGAV
1171 (alpha v integrins) bind SPP1 (osteopontin) to support trophoblast cell adhesion.
1172 *Reproduction* **153**, 695-706, doi:10.1530/REP-17-0043 (2017).

1173 85 Erikson, D. W., Burghardt, R. C., Bayless, K. J. & Johnson, G. A. Secreted
1174 phosphoprotein 1 (SPP1, osteopontin) binds to integrin alpha v beta 6 on porcine
1175 trophectoderm cells and integrin alpha v beta 3 on uterine luminal epithelial
1176 cells, and promotes trophectoderm cell adhesion and migration. *Biol Reprod* **81**,
1177 814-825, doi:10.1095/biolreprod.109.078600 (2009).

1178 86 Vallejo, J. *et al.* Activation of immune responses against the basement
1179 membrane component collagen type IV does not affect the development of
1180 atherosclerosis in ApoE-deficient mice. *Sci Rep* **9**, 5964, doi:10.1038/s41598-
1181 019-42375-8 (2019).

1182 87 Li, M. *et al.* Signaling pathways in macrophages: molecular mechanisms and
1183 therapeutic targets. *MedComm (2020)* **4**, e349, doi:10.1002/mco2.349 (2023).

1184 88 Ruytinx, P., Proost, P., Van Damme, J. & Struyf, S. Chemokine-Induced
1185 Macrophage Polarization in Inflammatory Conditions. *Front Immunol* **9**, 1930,
1186 doi:10.3389/fimmu.2018.01930 (2018).

1187 89 Furuhashi, M., Saitoh, S., Shimamoto, K. & Miura, T. Fatty Acid-Binding
1188 Protein 4 (FABP4): Pathophysiological Insights and Potent Clinical Biomarker
1189 of Metabolic and Cardiovascular Diseases. *Clin Med Insights Cardiol* **8**, 23-33,

1190 doi:10.4137/CMC.S17067 (2014).

1191 90 Wieczorek, E. *et al.* The Differential Effects of HDL Subpopulations on
1192 Lipoprotein Lipase (LPL)-Mediated VLDL Catabolism. *Biomedicines* **9**,
1193 doi:10.3390/biomedicines9121839 (2021).

1194 91 Fang, F. *et al.* Cathepsin K contributed to disturbed flow-induced
1195 atherosclerosis is dependent on integrin-actin cytoskeleton-NF-kappaB pathway.
1196 *Genes Dis* **10**, 583-595, doi:10.1016/j.gendis.2022.03.020 (2023).

1197 92 Zhang, H. *et al.* GPNMB plays an active role in the M1/M2 balance. *Tissue Cell*
1198 **74**, 101683, doi:10.1016/j.tice.2021.101683 (2022).

1199 93 Wang, J. *et al.* Macrophage-derived GPNMB trapped by fibrotic extracellular
1200 matrix promotes pulmonary fibrosis. *Commun Biol* **6**, 136, doi:10.1038/s42003-
1201 022-04333-5 (2023).

1202 94 Nickl, B., Qadri, F. & Bader, M. Role of Gpnmb in atherosclerosis of female
1203 mice. *Biochem Biophys Res Commun* **621**, 20-24,
1204 doi:10.1016/j.bbrc.2022.06.082 (2022).

1205 95 Chen, P. *et al.* Identification and validation of four hub genes involved in the
1206 plaque deterioration of atherosclerosis. *Aging (Albany NY)* **11**, 6469-6489,
1207 doi:10.18632/aging.102200 (2019).

1208 96 Huang, K. *et al.* Serum secreted phosphoprotein 1 level is associated with
1209 plaque vulnerability in patients with coronary artery disease. *Front Immunol* **15**,
1210 1285813, doi:10.3389/fimmu.2024.1285813 (2024).

1211 97 Orecchioni, M., Ghosheh, Y., Pramod, A. B. & Ley, K. Macrophage Polarization:
1212 Different Gene Signatures in M1(LPS+) vs. Classically and M2(LPS-) vs.
1213 Alternatively Activated Macrophages. *Front Immunol* **10**, 1084,
1214 doi:10.3389/fimmu.2019.01084 (2019).

1215 98 Collison, J. MMP12 makes the cut. *Nat Rev Rheumatol* **14**, 501,
1216 doi:10.1038/s41584-018-0056-y (2018).

1217 99 Dean, R. A. *et al.* Macrophage-specific metalloelastase (MMP-12) truncates and
1218 inactivates ELR+ CXC chemokines and generates CCL2, -7, -8, and -13
1219 antagonists: potential role of the macrophage in terminating polymorphonuclear
1220 leukocyte influx. *Blood* **112**, 3455-3464, doi:10.1182/blood-2007-12-129080
1221 (2008).

1222 100 Willemsen, L. & de Winther, M. P. Macrophage subsets in atherosclerosis as
1223 defined by single-cell technologies. *J Pathol* **250**, 705-714,

1224 doi:10.1002/path.5392 (2020).

1225 101 Chen, Y., Zhang, J., Cui, W. & Silverstein, R. L. CD36, a signaling receptor and
1226 fatty acid transporter that regulates immune cell metabolism and fate. *J Exp Med*
1227 **219**, doi:10.1084/jem.20211314 (2022).

1228 102 Herrmann, J., Lerman, L. O., Mukhopadhyay, D., Napoli, C. & Lerman, A.
1229 Angiogenesis in atherogenesis. *Arterioscler Thromb Vasc Biol* **26**, 1948-1957,
1230 doi:10.1161/01.ATV.0000233387.90257.9b (2006).

1231 103 Khurana, R., Simons, M., Martin, J. F. & Zachary, I. C. Role of angiogenesis in
1232 cardiovascular disease: a critical appraisal. *Circulation* **112**, 1813-1824,
1233 doi:10.1161/CIRCULATIONAHA.105.535294 (2005).

1234 104 Asrih, M. *et al.* Overview of growth differentiation factor 15 in metabolic
1235 syndrome. *J Cell Mol Med* **27**, 1157-1167, doi:10.1111/jcmm.17725 (2023).

1236 105 Adela, R. & Banerjee, S. K. GDF-15 as a Target and Biomarker for Diabetes
1237 and Cardiovascular Diseases: A Translational Prospective. *J Diabetes Res* **2015**,
1238 490842, doi:10.1155/2015/490842 (2015).

1239 106 Kempf, T. *et al.* The transforming growth factor-beta superfamily member
1240 growth-differentiation factor-15 protects the heart from ischemia/reperfusion
1241 injury. *Circ Res* **98**, 351-360, doi:10.1161/01.RES.0000202805.73038.48
1242 (2006).

1243 107 Preusch, M. R. *et al.* GDF-15 protects from macrophage accumulation in a
1244 mousemodel of advanced atherosclerosis. *Eur J Med Res* **18**, 19,
1245 doi:10.1186/2047-783X-18-19 (2013).

1246 108 Kempf, T. *et al.* GDF-15 is an inhibitor of leukocyte integrin activation required
1247 for survival after myocardial infarction in mice. *Nat Med* **17**, 581-588,
1248 doi:10.1038/nm.2354 (2011).

1249 109 Johnen, H. *et al.* Increased expression of the TGF-b superfamily cytokine MIC-
1250 1/GDF15 protects ApoE(-/-) mice from the development of atherosclerosis.
1251 *Cardiovasc Pathol* **21**, 499-505, doi:10.1016/j.carpath.2012.02.003 (2012).

1252 110 Cai, X. *et al.* High-Density Lipoprotein (HDL) Inhibits Serum Amyloid A
1253 (SAA)-Induced Vascular and Renal Dysfunctions in Apolipoprotein E-Deficient
1254 Mice. *Int J Mol Sci* **21**, doi:10.3390/ijms21041316 (2020).

1255 111 Hao, Y. *et al.* Integrated analysis of multimodal single-cell data. *Cell* **184**, 3573-
1256 3587 e3529, doi:10.1016/j.cell.2021.04.048 (2021).

112 Yu, G., Wang, L. G., Han, Y. & He, Q. Y. clusterProfiler: an R package for comparing biological themes among gene clusters. *OMICS* **16**, 284-287, doi:10.1089/omi.2011.0118 (2012).

113 Jin, S. *et al.* Inference and analysis of cell-cell communication using CellChat. *Nat Commun* **12**, 1088, doi:10.1038/s41467-021-21246-9 (2021).

Figure 1

a

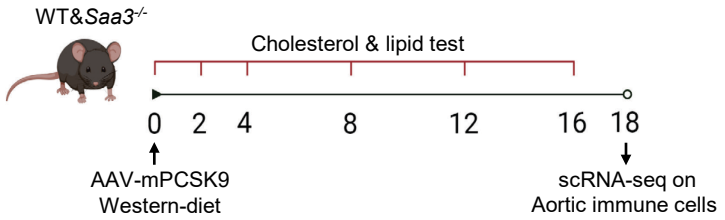

b

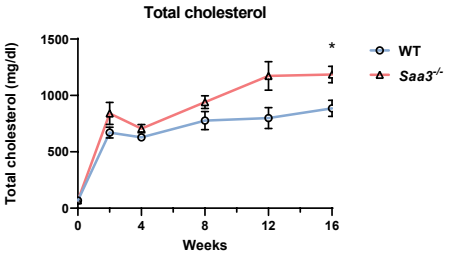

c

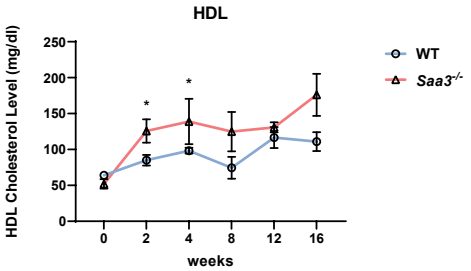

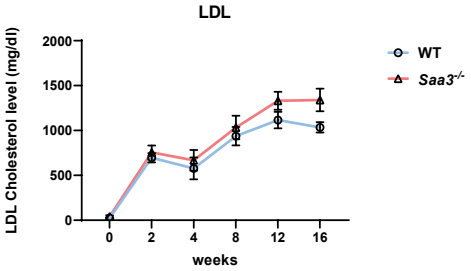

d

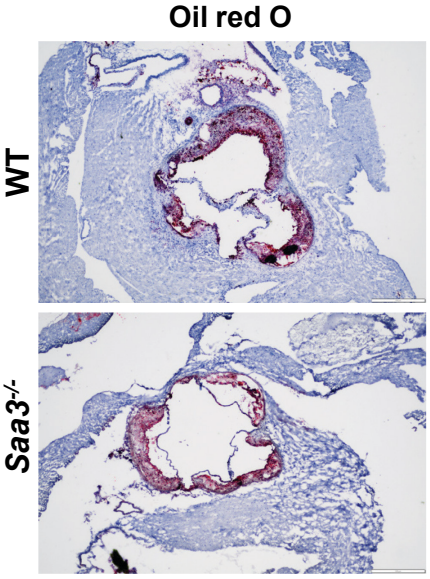

e

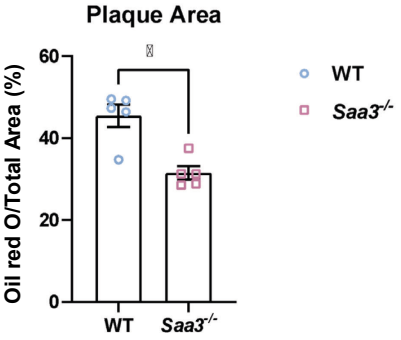

Figure 2

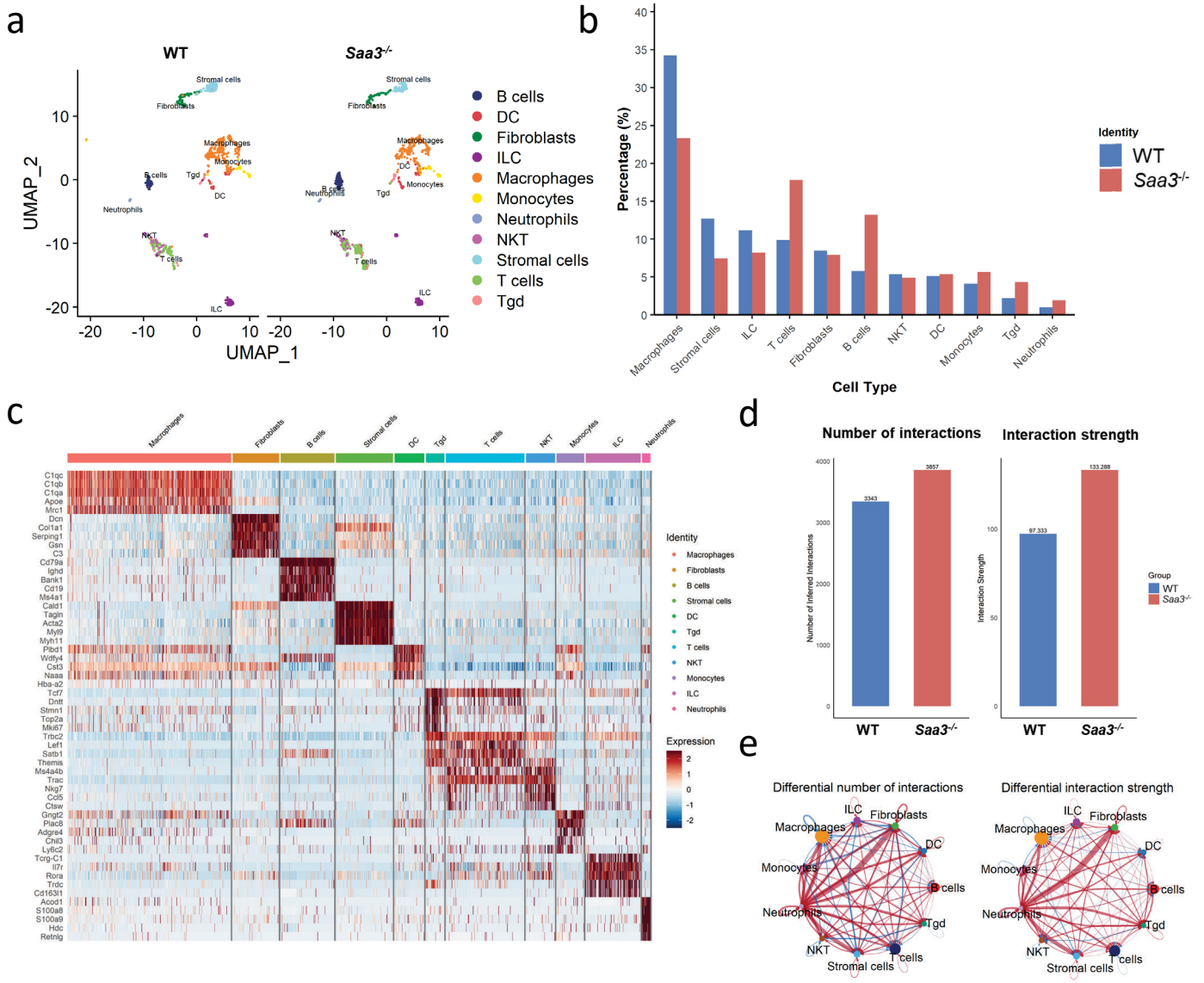
a
WT
Saa3-/-
UMAP_2
UMAP_1
Stromal cells
Fibroblasts
Macrophages
Monocytes
B cells
Tgd
DC
Neutrophils
NKT
T cells
ILC
B cells
DC
Fibroblasts
ILC
Macrophages
Monocytes
Neutrophils
NKT
Stromal cells
T cells
Tgd
b
Percentage (%)
Cell Type
Macrophages
Stromal cells
ILC
T cells
Fibroblasts
B cells
NKT
DC
Monocytes
Tgd
Neutrophils
Identity
WT
Saa3-/-
c
Macrophages
Fibroblasts
B cells
Stromal cells
DC
Tgd
T cells
NKT
Monocytes
ILC
Neutrophils
Identity
Expression
d
Number of interactions
Interaction strength
Number of Inferred Interactions
Interaction Strength
3343
3857
97.333
133.288
WT
Saa3-/-
Group
e
Differential number of interactions
Differential interaction strength
ILC
Fibroblasts
Macrophages
DC
Monocytes
B cells
Neutrophils
Tgd
NKT
T cells
Stromal cells
f
Differential number of interactions
Differential interaction strength
Sources (Sender)
B cells
DC
Fibroblasts
ILC
Macrophages
Monocyte
Neutrophils
NKT
Stromal cells
T cells
Tgd
Relative values

Figure 3

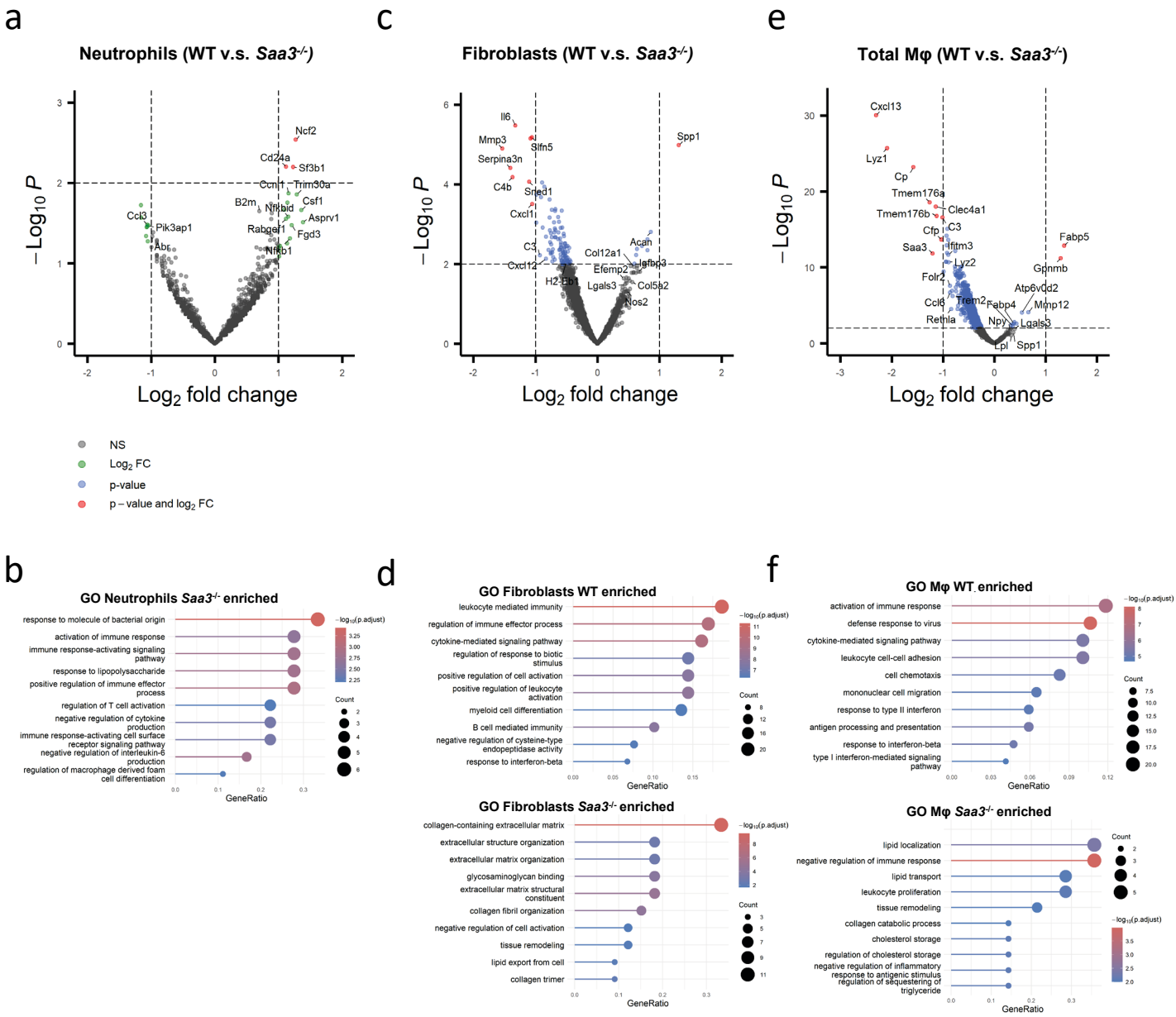
a
Neutrophils (WT v.s. Saa3-/-)
Ncf2
Cd24a
Sf3b1
Ccnl1
Trim30a
B2m
Nfkbid
Csf1
Ccl3
Pik3ap1
Asprv1
Rabgef1
Fgd3
Abr
Nfkb1
−Log10 P
Log2 fold change
c
Fibroblasts (WT v.s. Saa3-/-)
Il6
Mmp3
Slfn5
Serpina3n
C4b
Sned1
Cxcl1
C3
Cxcl12
H2-Eb1
Spp1
Acan
Col12a1
Igfbp3
Efemp2
Lgals3
Col5a2
Nos2
−Log10 P
Log2 fold change
e
Total Mφ (WT v.s. Saa3-/-)
Cxcl13
Lyz1
Cp
Tmem176a
Tmem176b
Clec4a1
Cfp
C3
Saa3
Ifitm3
Lyz2
Folr2
Ccl6
Trem2
Rethla
Fabp5
Gpnmb
Atp6v0d2
Fabp4
Mmp12
Npy
Lgals3
Lpl
Spp1
−Log10 P
Log2 fold change
NS
Log2 FC
p-value
p – value and log2 FC
b
GO Neutrophils Saa3-/- enriched
response to molecule of bacterial origin
activation of immune response
immune response-activating signaling pathway
response to lipopolysaccharide
positive regulation of immune effector process
regulation of T cell activation
negative regulation of cytokine production
immune response-activating cell surface receptor signaling pathway
negative regulation of interleukin-6 production
regulation of macrophage derived foam cell differentiation
−log10(p.adjust)
Count
GeneRatio
d
GO Fibroblasts WT enriched
leukocyte mediated immunity
regulation of immune effector process
cytokine-mediated signaling pathway
regulation of response to biotic stimulus
positive regulation of cell activation
positive regulation of leukocyte activation
myeloid cell differentiation
B cell mediated immunity
negative regulation of cysteine-type endopeptidase activity
response to interferon-beta
−log10(p.adjust)
Count
GeneRatio
GO Fibroblasts Saa3-/- enriched
collagen-containing extracellular matrix
extracellular structure organization
extracellular matrix organization
glycosaminoglycan binding
extracellular matrix structural constituent
collagen fibril organization
negative regulation of cell activation
tissue remodeling
lipid export from cell
collagen trimer
−log10(p.adjust)
Count
GeneRatio
f
GO Mφ WT enriched
activation of immune response
defense response to virus
cytokine-mediated signaling pathway
leukocyte cell-cell adhesion
cell chemotaxis
mononuclear cell migration
response to type II interferon
antigen processing and presentation
response to interferon-beta
type I interferon-mediated signaling pathway
−log10(p.adjust)
Count
GeneRatio
GO Mφ Saa3-/- enriched
lipid localization
negative regulation of immune response
lipid transport
leukocyte proliferation
tissue remodeling
collagen catabolic process
cholesterol storage
regulation of cholesterol storage
negative regulation of inflammatory response to antigenic stimulus
regulation of sequestering of triglyceride
Count
−log10(p.adjust)
GeneRatio

Figure 4

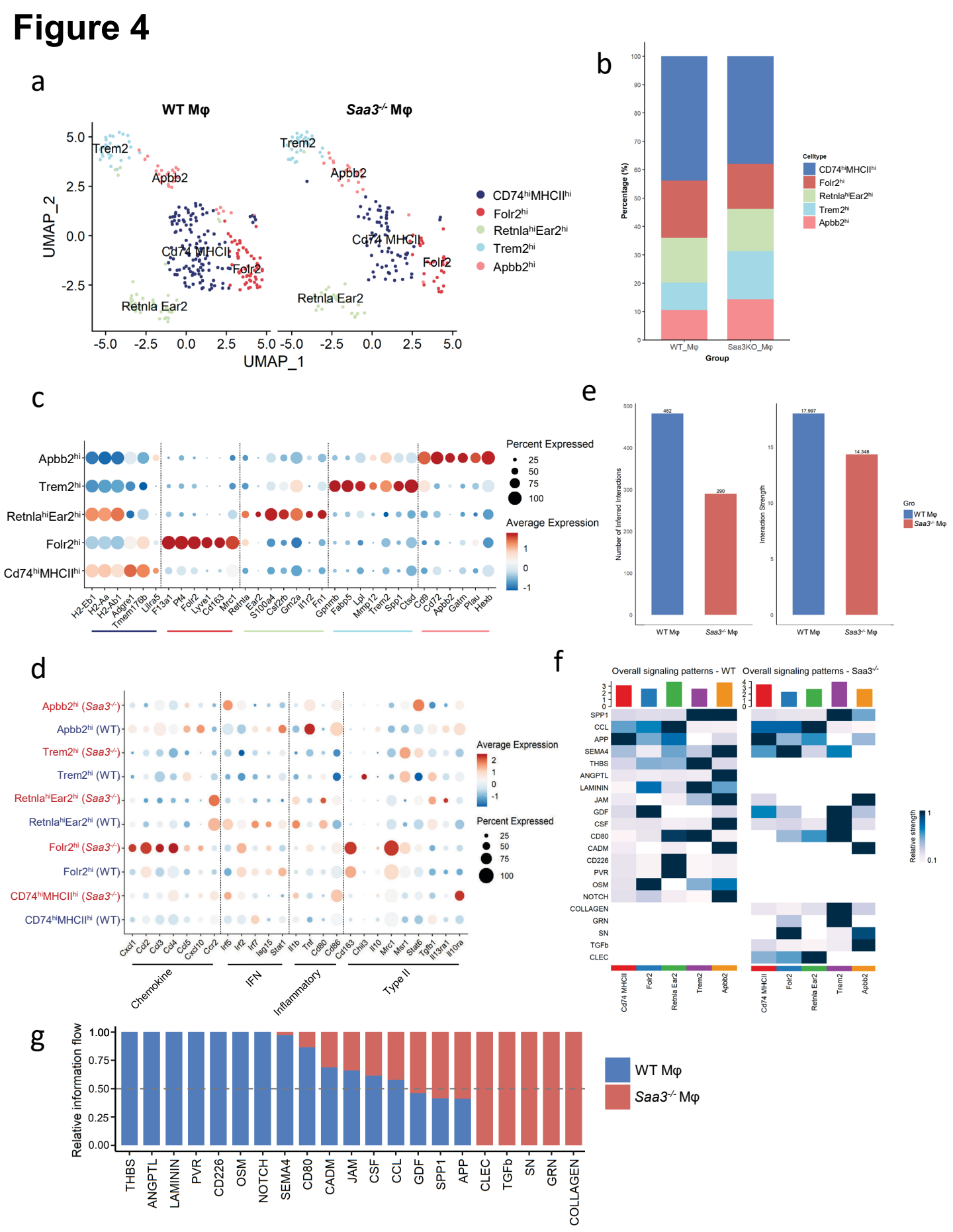
a
WT Mφ
Saa3-/- Mφ
Trem2
Apbb2
Cd74 MHCII
Folr2
Retnla Ear2
UMAP_2
UMAP_1
CD74hiMHCIIhi
Folr2hi
RetnlahiEar2hi
Trem2hi
Apbb2hi
b
Percentage (%)
Group
WT_Mφ
Saa3KO_Mφ
Celltype
c
Percent Expressed
Average Expression
d
Chemokine
IFN
Inflammatory
Type II
e
Number of Inferred Interactions
Interaction Strength
482
290
17.997
14.348
WT Mφ
Saa3-/- Mφ
f
Overall signaling patterns - WT
Overall signaling patterns - Saa3-/-
Relative strength
g
Relative information flow
WT Mφ
Saa3-/- Mφ

Figure 5

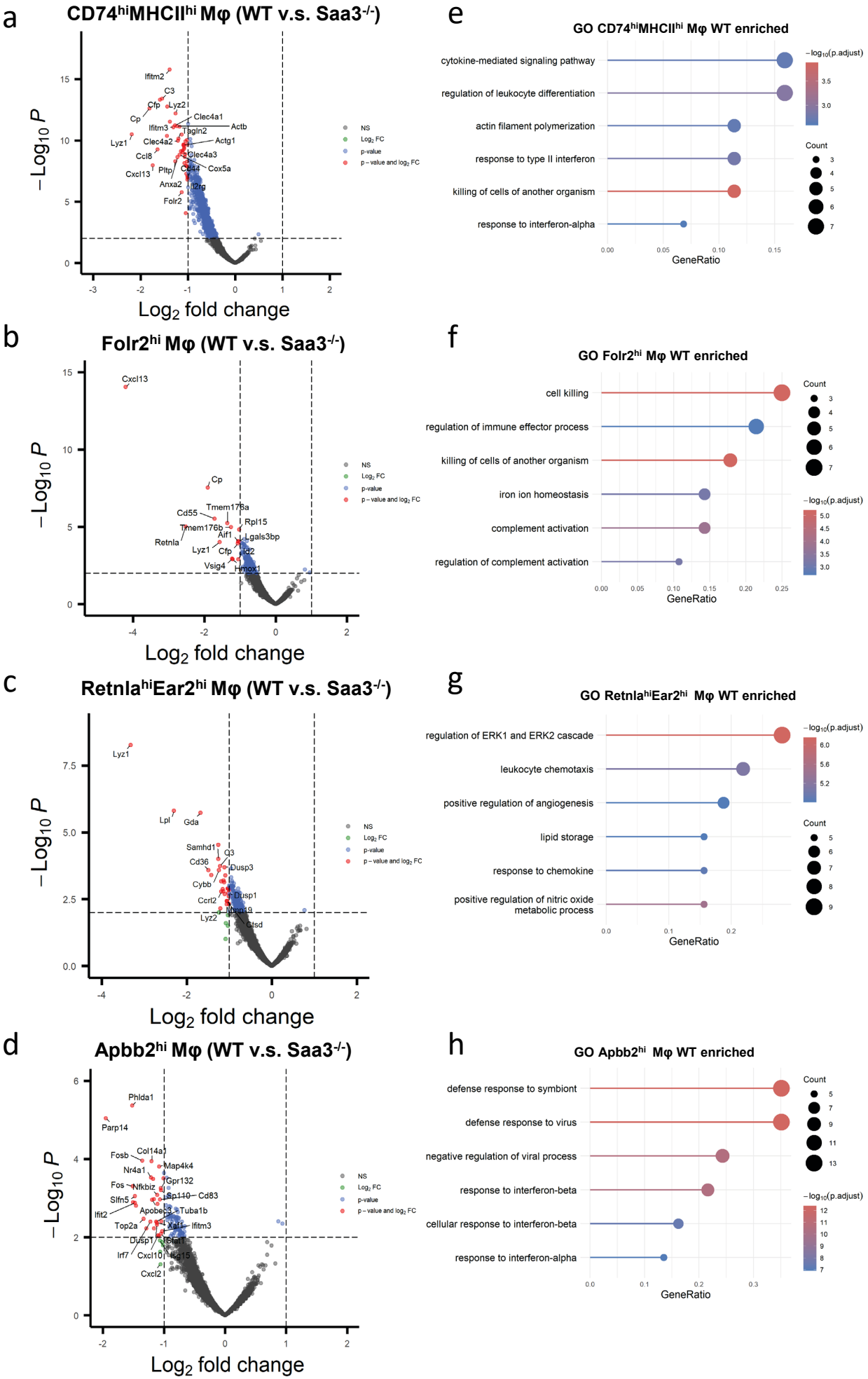
a
CD74hiMHCIIhi Mφ (WT v.s. Saa3-/-)
Ifitm2
C3
Cfp
Lyz2
Cp
Clec4a1
Ifitm3
Actb
Tagln2
Lyz1
Clec4a2
Actg1
Ccl8
Clec4a3
Cxcl13
Pltp
Cd44
Cox5a
Anxa2
Il2rg
Folr2
NS
Log2 FC
p-value
p – value and log2 FC
– Log10 P
Log2 fold change
b
Folr2hi Mφ (WT v.s. Saa3-/-)
Cxcl13
Cp
Tmem176a
Cd55
Rpl15
Tmem176b
Aif1
Lgals3bp
Retnla
Lyz1
Cfp
Id2
Vsig4
Hmox1
c
RetnlahiEar2hi Mφ (WT v.s. Saa3-/-)
Lyz1
Lpl
Gda
Samhd1
Q3
Cd36
Dusp3
Cybb
Ccrl2
Dusp1
Mxp19
Lyz2
Ctsd
d
Apbb2hi Mφ (WT v.s. Saa3-/-)
Phlda1
Parp14
Fosb
Col14a1
Nr4a1
Map4k4
Gpr132
Fos
Nfkbiz
Slfn5
Sp110
Cd83
Ifit2
Apobec3
Tuba1b
Top2a
Xaf1
Ifitm3
Dusp1
Isg15
Irf7
Cxcl10
Cxcl2
e
GO CD74hiMHCIIhi Mφ WT enriched
cytokine-mediated signaling pathway
regulation of leukocyte differentiation
actin filament polymerization
response to type II interferon
killing of cells of another organism
response to interferon-alpha
GeneRatio
–log10(p.adjust)
Count
f
GO Folr2hi Mφ WT enriched
cell killing
regulation of immune effector process
killing of cells of another organism
iron ion homeostasis
complement activation
regulation of complement activation
GeneRatio
Count
–log10(p.adjust)
g
GO RetnlahiEar2hi Mφ WT enriched
regulation of ERK1 and ERK2 cascade
leukocyte chemotaxis
positive regulation of angiogenesis
lipid storage
response to chemokine
positive regulation of nitric oxide metabolic process
GeneRatio
–log10(p.adjust)
Count
h
GO Apbb2hi Mφ WT enriched
defense response to symbiont
defense response to virus
negative regulation of viral process
response to interferon-beta
cellular response to interferon-beta
response to interferon-alpha
GeneRatio
Count
–log10(p.adjust)

Figure 6

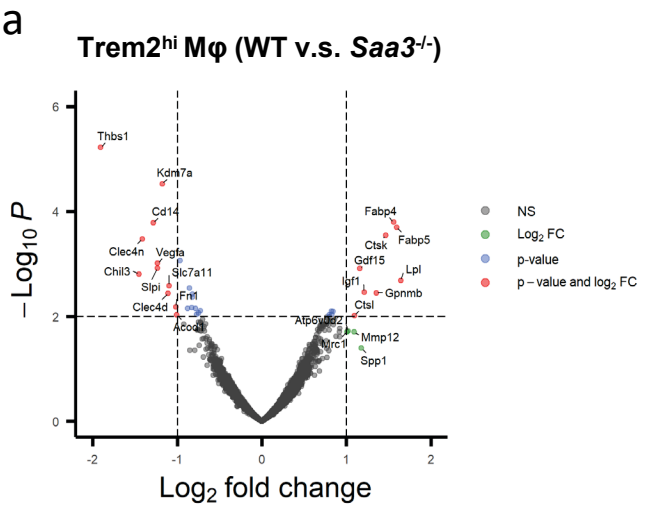
a
Trem2hi Mφ (WT v.s. Saa3-/-)
Thbs1
Kdm7a
Cd14
Clec4n
Vegfa
Chil3
Slc7a11
Slpi
Fmf
Clec4d
Acod1
Fabp4
Fabp5
Ctsk
Gdf15
Lpl
Igf1
Gpnmb
Ctsl
Apoe
Mrc1
Mmp12
Spp1
NS
Log2 FC
p-value
p – value and log2 FC
– Log10 P
Log2 fold change

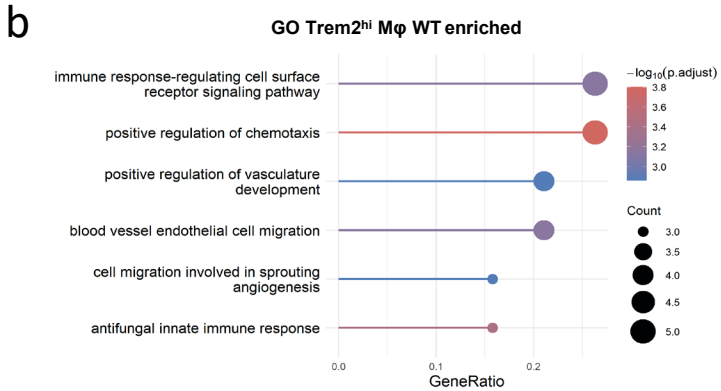
b
GO Trem2hi Mφ WT enriched
immune response-regulating cell surface receptor signaling pathway
positive regulation of chemotaxis
positive regulation of vasculature development
blood vessel endothelial cell migration
cell migration involved in sprouting angiogenesis
antifungal innate immune response
GeneRatio
– log10(p.adjust)
Count

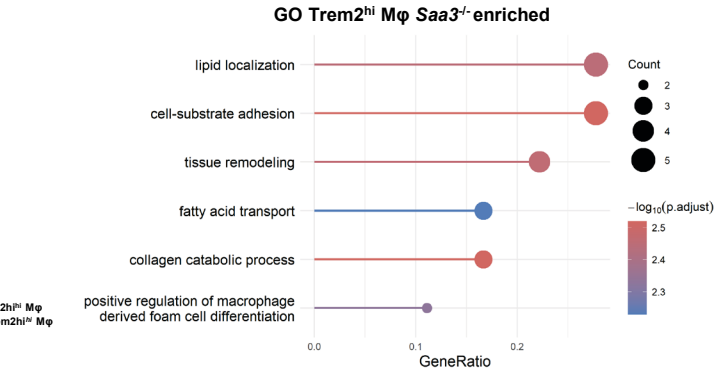
GO Trem2hi Mφ Saa3-/- enriched
lipid localization
cell-substrate adhesion
tissue remodeling
fatty acid transport
collagen catabolic process
positive regulation of macrophage derived foam cell differentiation
GeneRatio
Count
– log10(p.adjust)

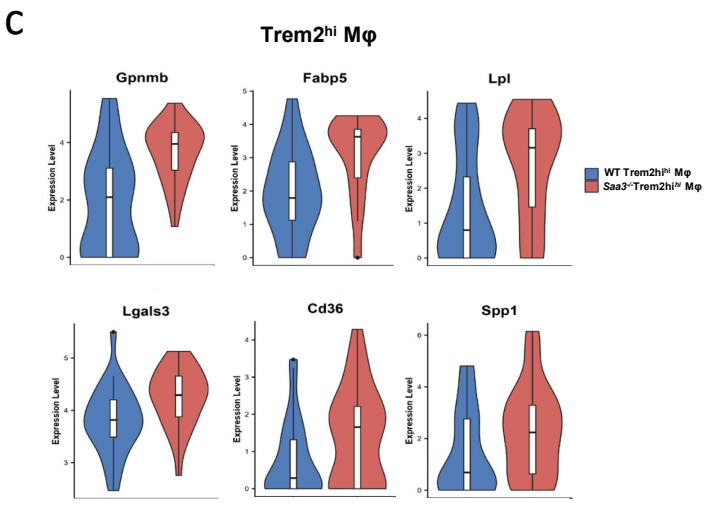
c
Trem2hi Mφ
Gpnmb
Fabp5
Lpl
Lgals3
Cd36
Spp1
Expression Level
WT Trem2hi Mφ
Saa3-/-Trem2hi Mφ

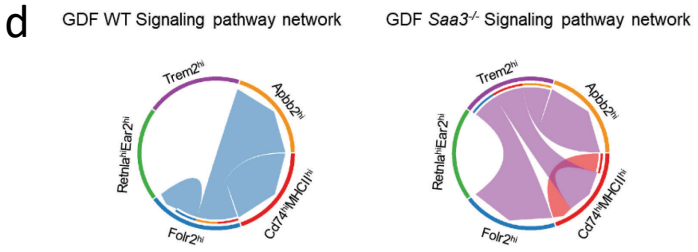
d
GDF WT Signaling pathway network
GDF Saa3-/- Signaling pathway network
Trem2hi
Apbb2hi
Cd74hiMHCIIhi
Folr2hi
Retnlahi Ear2hi

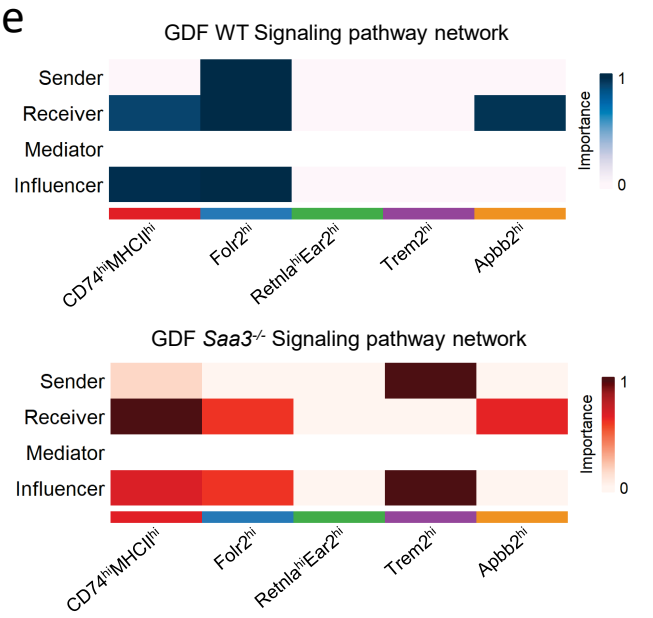
e
GDF WT Signaling pathway network
GDF Saa3-/- Signaling pathway network
Sender
Receiver
Mediator
Influencer
Importance
CD74hiMHCIIhi
Folr2hi
Retnlahi Ear2hi
Trem2hi
Apbb2hi

Supplementary Figure 1

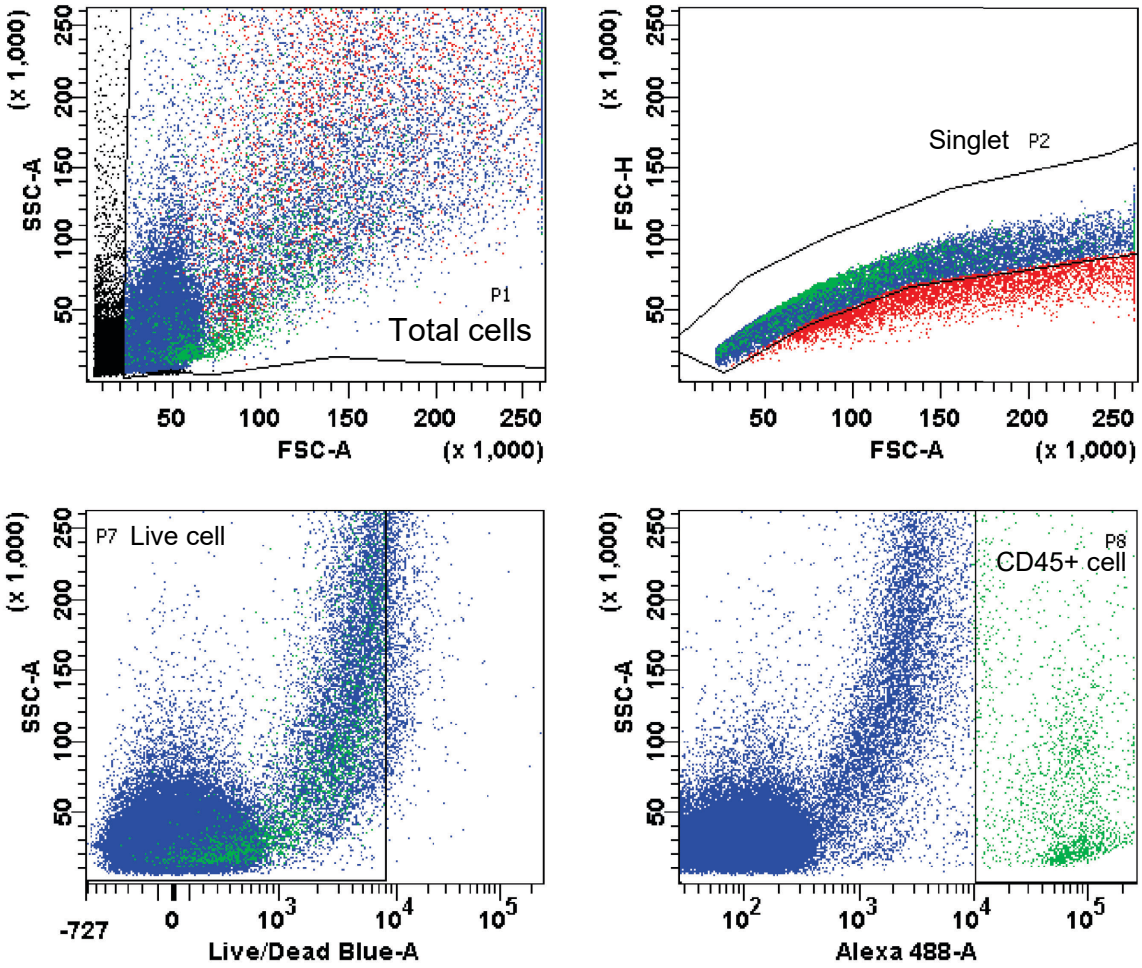

Supplementary Figure 2

a

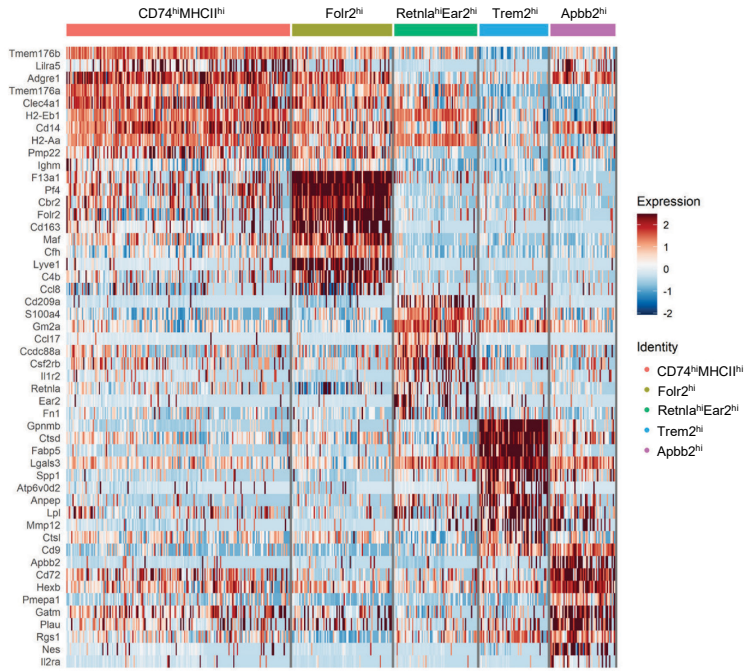

b

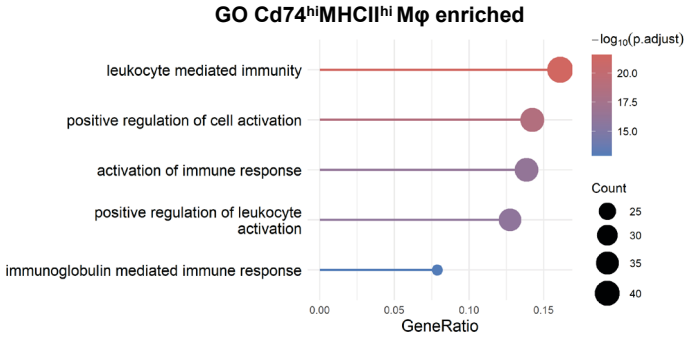

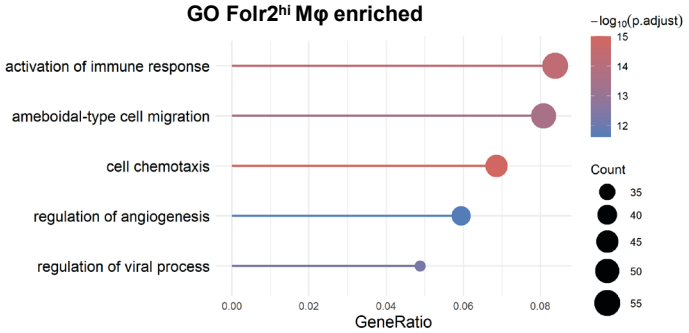

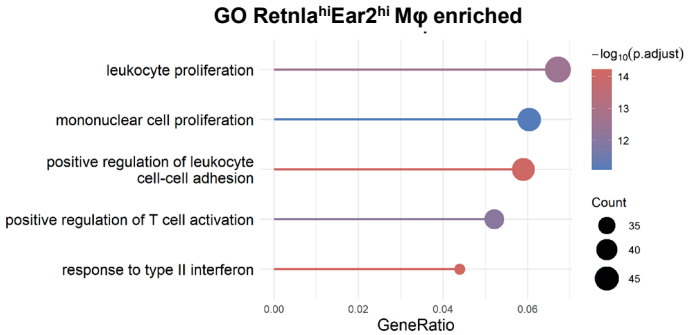

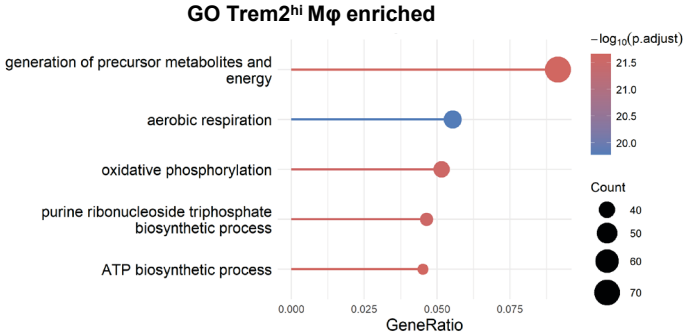

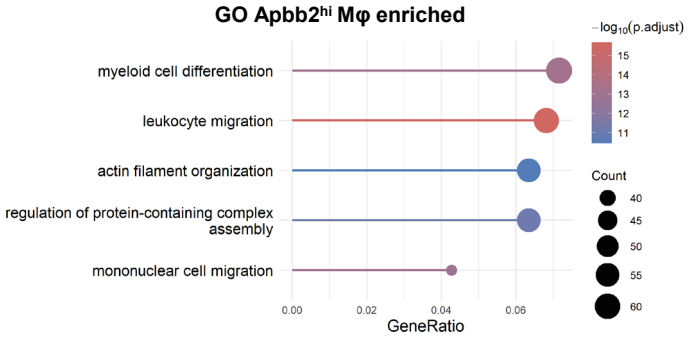

Supplementary Figure 3

a

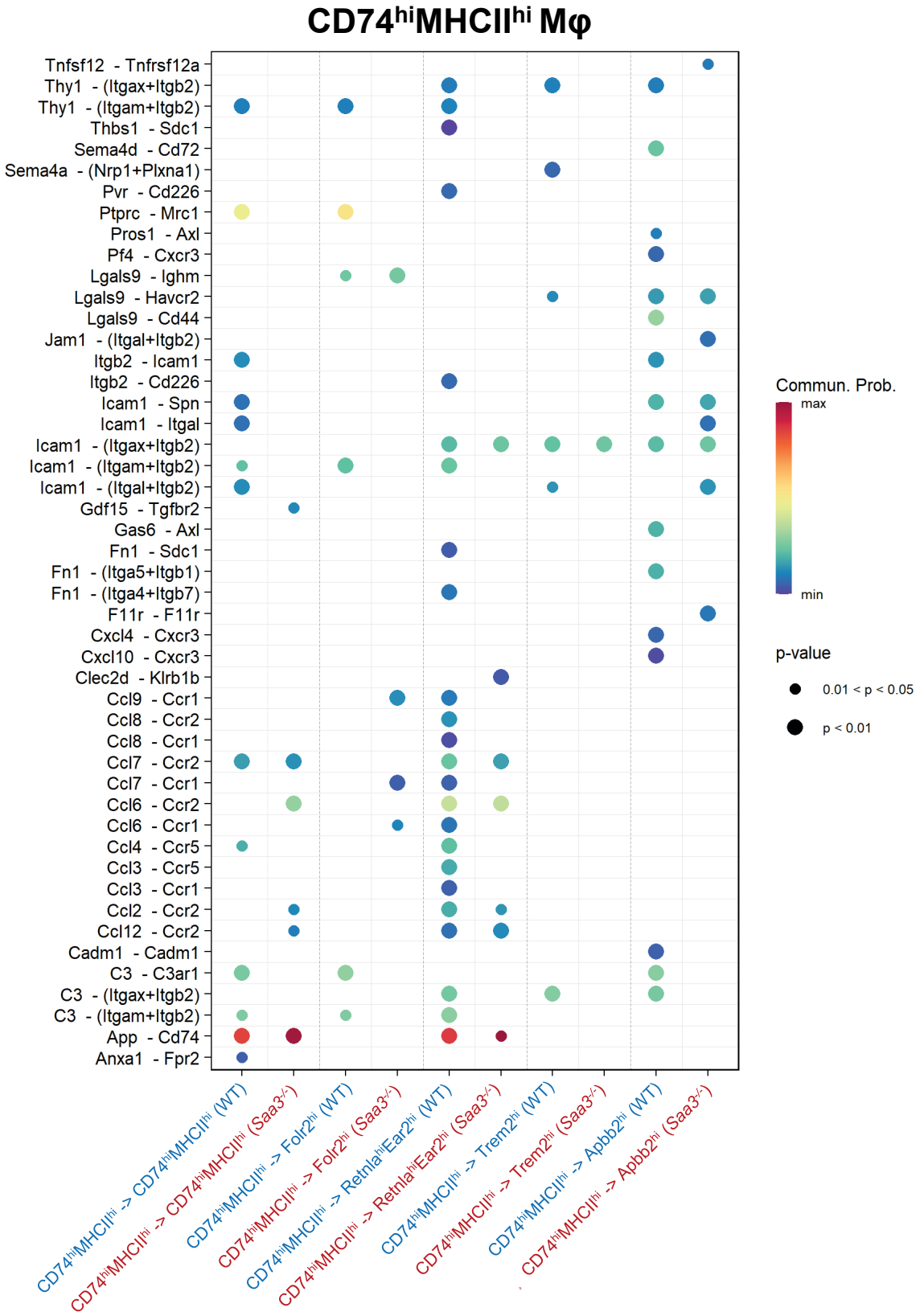

Supplementary Figure 3

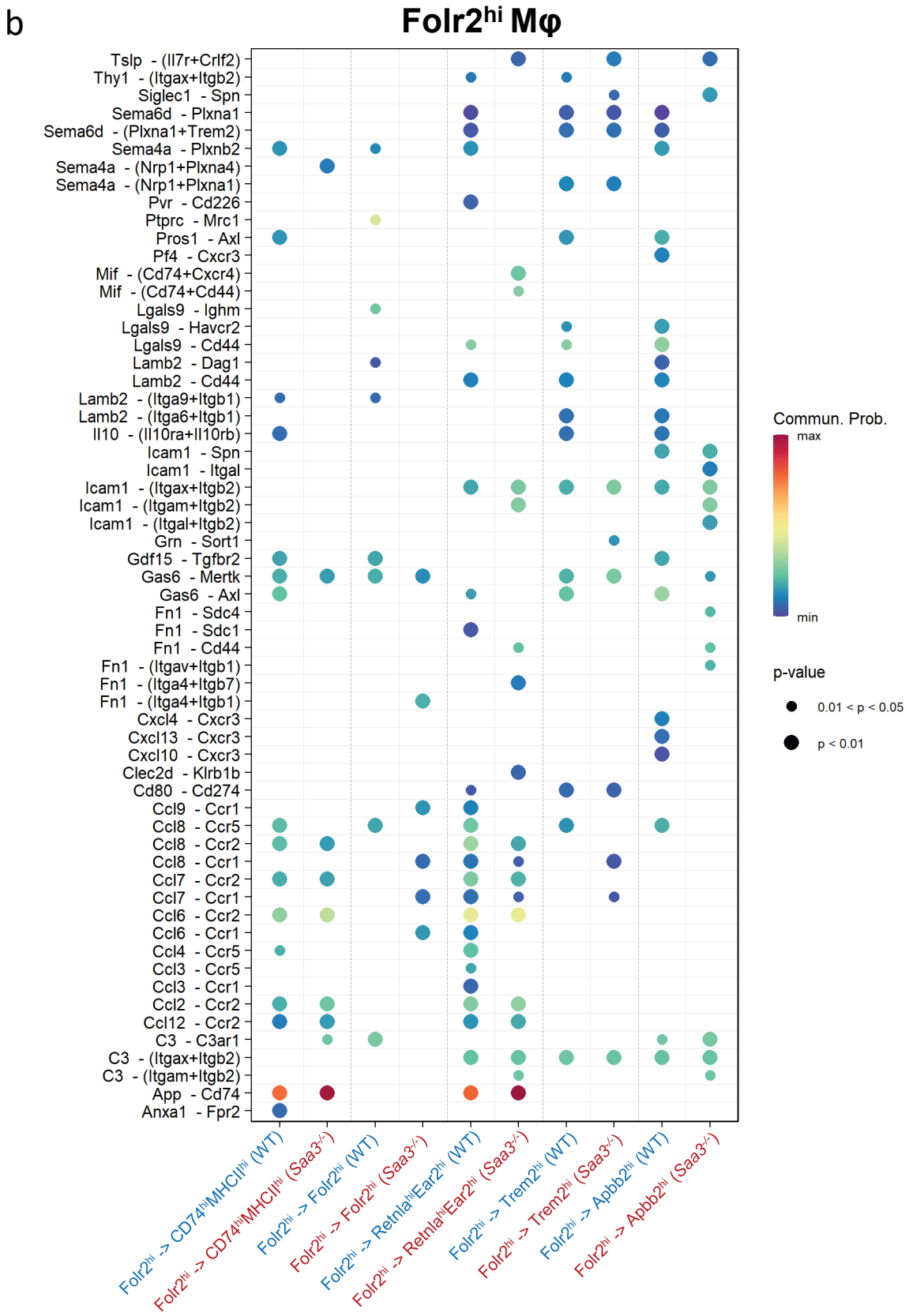

Supplementary Figure 3

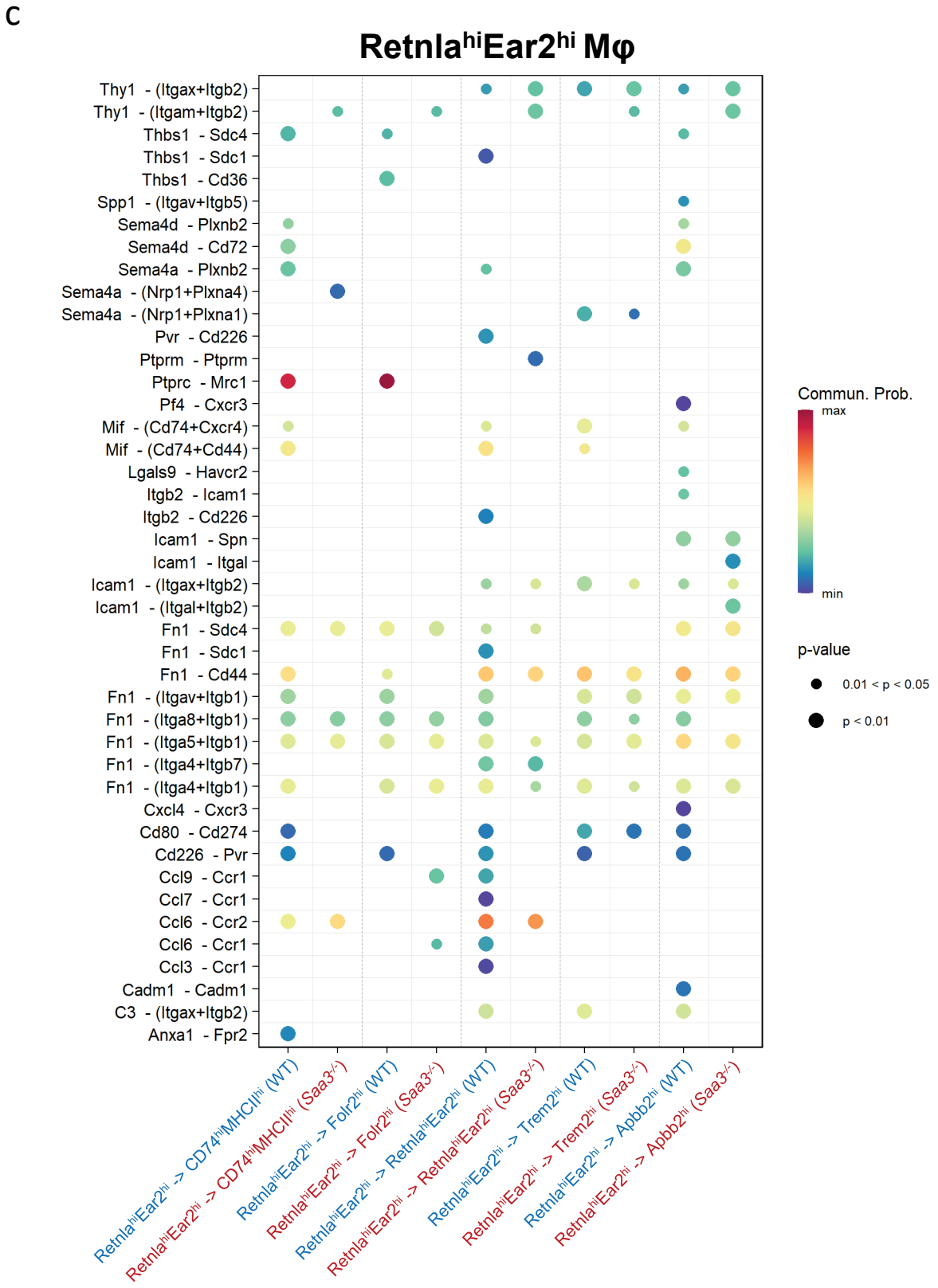

Supplementary Figure 3

d

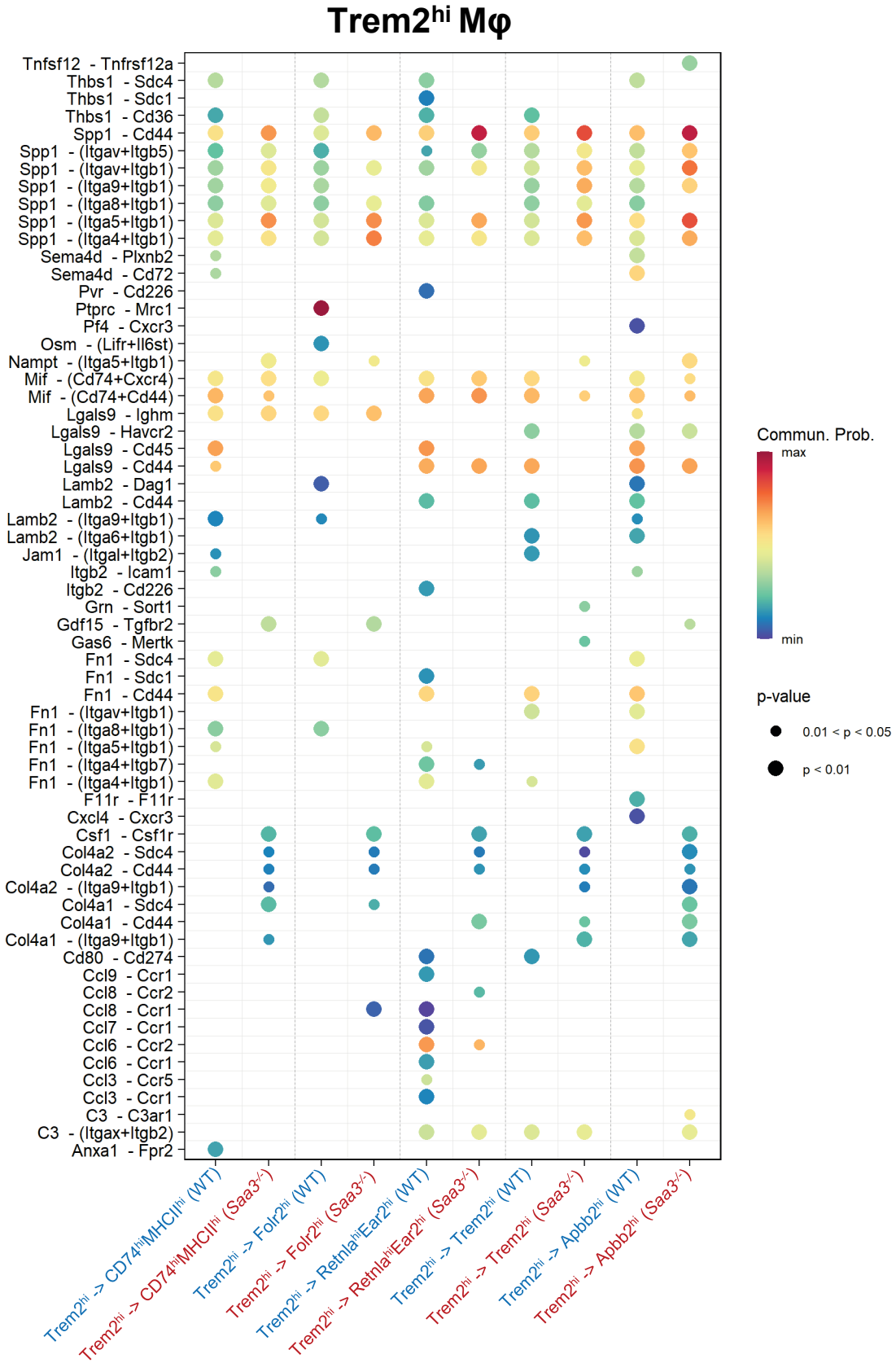

Supplementary Figure 3

e

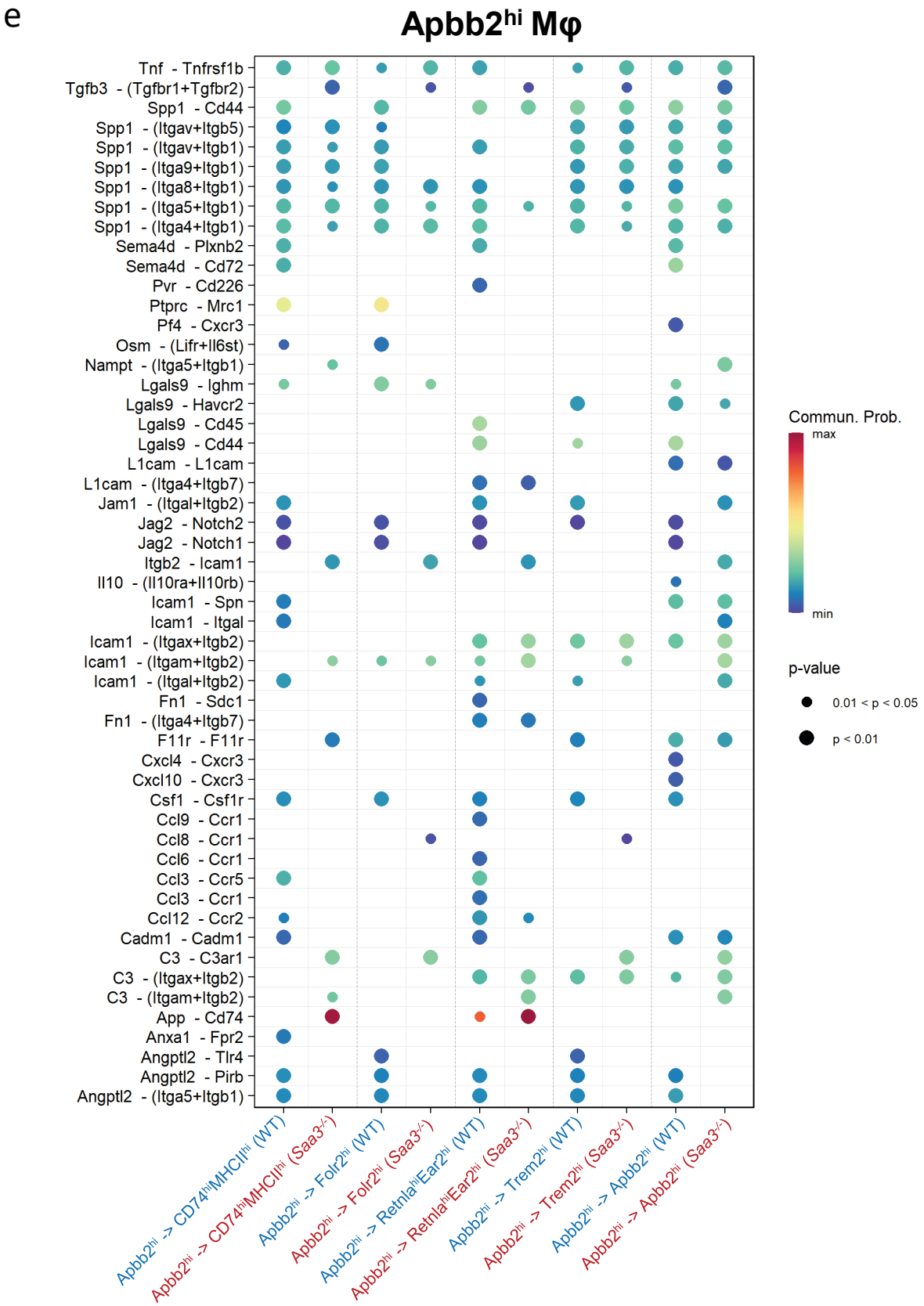
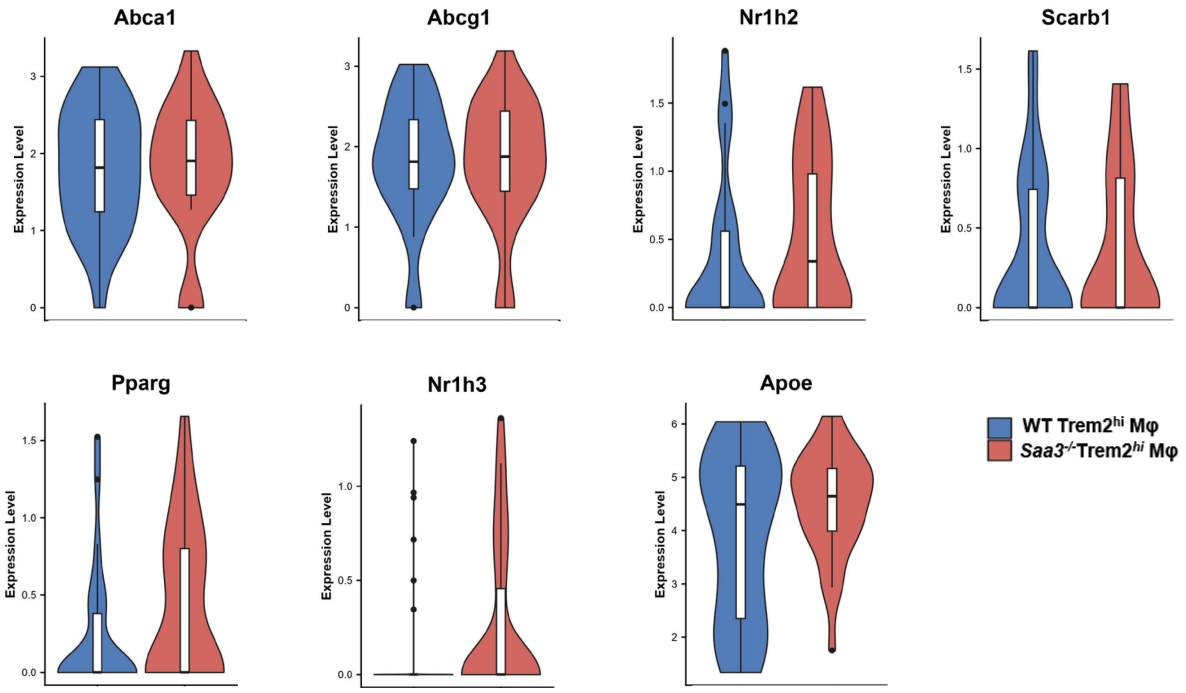
Supplementary Figure 4